FR4 Based Electromagnetic Energy Harvesters for Wireless Sensor Nodes

by

Gökhan Hatipoğlu

A Thesis Submitted to the
Graduate School of Engineering
in Partial Fulfillment of the Requirements for
the Degree of

Master of Science
in
Mechanical Engineering

Koc University
August 2009

Koc University

Graduate School of Sciences and Engineering

This is to certify that I have examined this copy of a master's thesis by

Gökhan Hatipoğlu

and have found that it is complete and satisfactory in all respects,
and that any and all revisions required by the final
examining committee have been made.

Committee Members:

_____

Erdem Alaca, Ph. D. (Advisor)

_____

Hakan Ürey, Ph. D. (Co-Advisor)

_____

İsmail Lazoğlu , Ph. D.

_____

Murat Sözer , Ph. D.

_____

Alper Kiraz , Ph. D.

Date: _____

ABSTRACT

Wireless Sensor Nodes are used for environment monitoring in many engineering applications. Powering these small sensors with battery is not reasonable due to regular replacement needs and the added size and mass of the batteries. Therefore, these sensors could be powered with environmental vibrations sources via vibration-to-electrical energy harvesters. Electromagnetic (EM) energy harvesting seems to be one of the most promising ways to power wireless sensors in a wireless sensor network. In this thesis, FR4, the most commonly used printed circuit board (PCB) material, is utilized as a mechanical vibrating structure for EM energy harvesting to power body worn sensors and intelligent tire sensors. The fundamental property of such vibration sources are that even though the impact frequency is relatively low, the signal is nearly periodic, the impact duration is short, and the vibration signal is rich in harmonic content. FR4 can be a better material for such applications compared to Silicon MEMS devices due to lower stiffness and broadband response. In order to demonstrate FR4 performance and broadband response, moving magnet type EM generator designs are developed and investigated throughout this work. A magneto-electro mechanical simulation model including the magnetic damping effects is developed and the results agree well with the experimental results. Human running acceleration at hip area that is obtained experimentally is simulated in order to demonstrate system performance, which results in a scavenged power of about 40 μW with 15 m/s^2 acceleration input. Mechanical stopper structures are built in the energy harvester design to limit the stress on suspension springs and to achieve efficient energy scavenging from nearly periodic and non-sinusoidal high-g excitations with rich harmonic content. For the intelligent tire applications, a compact FR4 scavenger designed that is able to withstand large shocks and vibrations due to non-linear mechanical shock stoppers built in the structure. Using our design, 0.4 mW power across a load resistance of 100Ω at off-

resonance operation is obtained in shaker experiments with limited acceleration input. In the actual operation, the tangential accelerations as a result of the tire-road contact are estimated to supply power around 1 mW with our design, which is sufficient for powering wireless tire sensors.

ÖZET

Kablosuz Sensör Düğümleri çevresel verileri incelemek üzere bir çok mühendislik uygulamalarında kullanılır. Batarya ile bu küçük sensörlere güç sağlamak mümkün değildir. Çünkü bataryanın düzenli değiştirme ihtiyacı ve büyüklüğü nedeniyle uzun süreli kullanımı bu sensörler için uygun değildir. Bu nedenle, bu sensörler çalışma ortamındaki titreşimi elektrik enerjisine harmanlama yoluyla ile beslenebilir. Elektromanyetik (EM) yolla elektrik enerjisi elde etmek, bir kablosuz sensör ağında bulunan kablosuz sensörleri beslemek için en umut verici yollarından biridir. Bu tezde, FR4, en yaygın olarak kullanılan bir baskı devre (PCB) malzemesi, vücuta giyilebilen sensörleri ve akıllı lastik sensörleri için EM enerji harmanlanması uygulamalarında mekanik bir titreşim yapısı olarak kullanılması önerilmektedir. Bu tarz titreşim kaynaklarının darbe frekansları düşük olmasına rağmen ve darbe müddeti kısa olmasına rağmen, harmonik içeriği oldukça zengindir. FR4 bu tür uygulamalar için Silikondan daha iyi bir malzeme olduğunu kanıtlamaktadır. Hareketli mıknatıs, sabit bobin tipli FR4 bazlı EM jeneratörlerin performansları ve geniş bant tepkileri bu çalışma boyunca deneylerle araştırıldı. Bu deneylere başlamadan önce bir manyetik-elektro-manyetik sayısal modeli de geliştirildi. Manyetik sönümleyici etkileri de bu simulasyon modeline dahil edildi . Daha sonra FR4 sistemi deneysel olarak elde edilen, koşan bir insanın kalça bölgesinde oluşan gerçek ivmelenme sinyalleri ile simule edildi. Numerik model, 15 m/s^2 ivme girişi ile 100 Ω luk yük direncinde 40 μW güç elde edildiğini tahmin etmektedir

FR4 yayların deplasmanını azaltmak için ve neredeyse periyodik ve sinusoid olmayan zengin harmonik içerikli yüksek şiddetteki ivmelenmelerden efektif enerji harmanlamasını sağlamak için mekanik durdurucu yapılar cihaza entegre edilmiştir.

Bu durdurucular daha sonra lineer olmayan bir şekilde tasarlanıp akıllı lastik uygulamaları için kompakt FR4 enerji üreticilerine büyük şoklara dayanıklı olacak şekilde entegre edilmiştir. Teker içinde oluşan gerçek yüzeysel kontak sinyalleri kullanılarak

yapılan deneylerde 100 Ω luk bir yük direnci üzerinde 0,4 mW güç elde edimiştir. Bu güç değeri çalkalayıcının frekans değerleri ile sınırlı kalmıştır. Gerçek teker operasyonunda güç değerlerinin 1 mW civarına ulaşacağı tahmin edilmektedir ki bu kablosuz sensor düğümleri için yeterli bir güç miktarıdır.

ACKNOWLEDGEMENTS

While being a master's student under mechanical engineering department, I had a chance to study in Optical MEMS laboratory (OML) which is under electrical engineering department. I am thus grateful to my advisors Prof. Erdem Alaca and Prof. Hakan Ürey for providing me this kind of special interdisciplinary research opportunity. With their creative ideas and guidance, I was able to develop my analytical thinking and problem solving techniques. It was a great opportunity for me to work in OML, which is a great facility.

I would like to thank Prof. Ipek Basdogan for providing access to mechanical shaker to perform my experiments. Also, I would like to thank Prof. İsmail Lazoğlu for letting me use CNC machines in his lab. I especially thank Selim Olcer for his effort on manufacturing my FR4 actuator designs in our facilities.

I would like to thank Prof. Ismail Lazoğlu, Prof. Murat Sözer and Prof. Alper Kiraz for kindly taking part in my thesis comitee.

I would like to thank all my friends and collegues from OML. I especially thank to Phc. Onur Ferhanoglu for participating in my experiments and for helping me whenever I needed. I am also grateful to Hüseyin Rahmi Seren. It was great to work in same environment and in some common projects. I am also glad to share quality time with Sertan Kutal Gökçe. I also thank all my OML members Erdem Erden, Aslıhan Arslan, Sven Hollström, Kishore and Duygu Kutluoğlu for being so great friends.

I also thank people who joined to Kocfutbol group. 9 months ago, we were just 5 guys loving to play soccer. As today, Kocfutbol members exceed 30 people. I am so lucky to play soccer every week with you guys.

I also thank to all my friends from Biochemistry lab.

Finally, my family… Anne, Baba ve kardeşim… I love you all. Life would be miserable without you. Thanks for your support.

LIST OF TABLES

LIST OF FIGURES

NOMENCLATURE

ε	Electromotive Force (EMF) in Volts.
ϕ	Magnetic Flux in Weber
N	Number of coil turns
$\vec{B}$	Magnetic Flux density in Tesla
A	Bobbin enclosed area
$y(t)$	Base displacement relative to ground
$x(t)$	Magnet displacement relative to ground
$z(t)$	Magnet displacement relative to base
k	Spring constant in N / m
c	Total damping coefficient
w_n	Natural frequency in rad / sec
θ_n	Phase angle
R_c	Coil Resistance
R_L	Load Resistance
L_c	Coil Inductance
A_p	Peak Acceleration of the base
V	Practical Volume of the energy harvester
F_m	Magnetic Damping Force
f_n	Natural Frequency of the FR4 based harvesters in Hertz.
Q	Mechanical Quality Factor
l_b	Total Beam Length
w_p	Pad width
Nd	Magnet type. Abbrevation for NdFeB.
B_R	Magnet Remanence

m	Magnet mass
R	Magnet radius
H	Magnet height
R_{ci}	Pick-up coil inner radius
R_{co}	Pick-up coil outer radius
a_t	Tangential Contact Acceleration
a_r	Radial Contact Acceleration
a_l	Lateral Contact Acceleration

Chapter 1

INTRODUCTION

Energy harvesting (or scavenging) means to extract any desired type of energy from the environmental sources like heat, light, noise, vibration and etc. Humans have been harvesting one form of energy to another for hundreds of years. The basic and maybe the oldest example is the windmills. Windmills use wind as a power source to produce energy in order to obtain flour for breads. The kinetic energy of the wind is harvested into useful power to rotate the grinders.

In numerous engineering applications, energy harvesting plays a key role. For example, the daily used vehicles and cars harvest the chemical energy stored in petroleum or gas into kinetic energy. Beside, kinetic energy of wild rivers is harvested into electrical energy in dams. Another important example is the wind turbines. Again the kinetic energy of the wind, which is an unlimited source of energy, is harvested into electrical power that is on the order of MW. The examples may grow, but the last two examples are much more interest to this work. They are electrical generators, which are devices that harvest mechanical energy into electrical energy via Faraday's Law of Induction that is explained in Chapter 3 in detail and it a basic way of producing electrical energy. This process of acquiring the energy surrounding a system and converting it into usable electrical energy is termed as "power harvesting" [1].

In recent years, alternative energy sources and energy producing techniques have already gained more importance due to scarcity of exhaustible energy sources like

petroleum, coal and natural gas. Moreover, the threat of global warming to the ecological system is increasing. Among these energy producing techniques, power harvesting is an extremely popular method, especially for portable electronics. Due to rapid advances in portable technology (laptops, cell phones, wireless sensors), battery power stays limited. Today's advanced technologies like disk capacity, CPU speed, available RAM improved by 1000 times since 1990s. However, battery energy density has improved only 10 times more [2]. In addition, battery life is very short for high power consuming technologies. Moreover, battery is bulky. While engineers design new electronic devices, most of the available design volume is allocated for batteries. In addition, batteries need regular replacements. All these facts are disadvantages for a battery.

Thus, some technologies do not prefer to perform regular replacements nor to allocate large volumes for batteries. Wireless sensor nodes, which are the main interests of this thesis, are one of those low power consuming electronic devices. They are autonomous and can operate in wireless sensor networks, which is shown in figure 1.1.

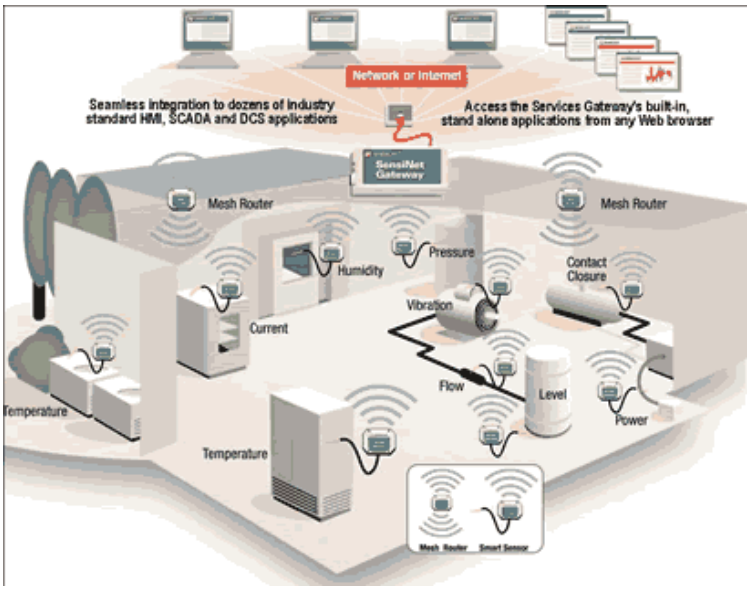

Figure 1.1 An example of wireless sensor network [3]

These nodes are generally used for monitoring environmental conditions like pressure, humidity, current, pollutants and etc. Since they are autonomous, they can communicate with each other forming a wireless sensor network (WSN). They can be used in harsh environments like in nuclear reactors in order to monitor radioactivity. In such applications, battery replacements may become impossible. Depending on the environment they are placed in, there can be environmental energy sources for harvesting their own power. By this way, they get rid of battery dependence.

One of the abundant environmental sources is the vibration that is investigated throughout this thesis. Nearly in every environment, vibrations may exist like in the cases of human motion and tire-road contacts, which are two basic application areas that the author of this paper is interested in. Body worn sensors and tire condition monitoring sensors are two kinds of wireless sensors. Body worn sensors deliver information about the human condition like heart beat rate, the external or internal body temperature and etc. Tire sensors monitor the slip angle, the temperature, the tire pressure and etc. These sensor nodes require very low powers to send informative signals like on the order of mW, so small sized electromagnetic generator units attached to them could be used as to power them. Once the sensors are spread or placed to the environment, they will harvest mechanical vibrations into electrical energy and will operate for an infinite time unless any hardware problem occurs. This kind of systems, which can power themselves through power harvesting can be sometimes called “self powered systems”. Figure 1.2 below shows a wireless sensor node developed by a group Berkeley University. The practical volume of the device is comparable to a finger size.

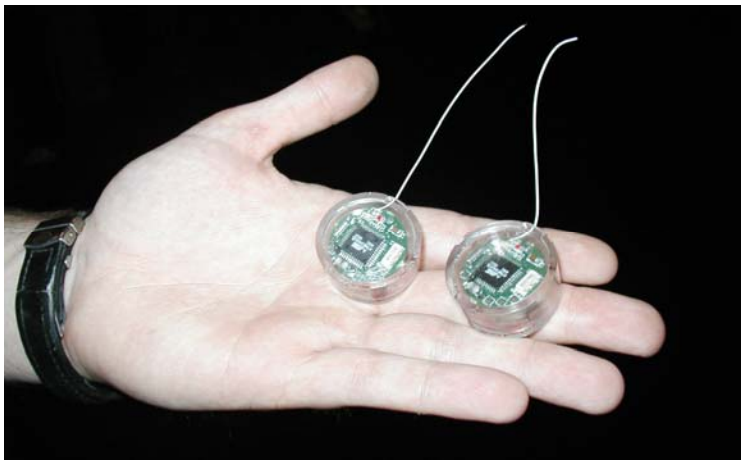

1.2 A wireless sensor node [4]

Since wireless sensor nodes are small scale devices, microscale power harvesting devices are first suggested. These Micro-Electro-Mechanical-Systems (MEMS) based electromagnetic devices are still popular today and a heavy research is going on. However, these devices have very high resonance frequencies. As it will be explained in Chapter 3, the optimum condition of power harvesting is to adjust the harvester resonance frequency to environmental vibration frequency. However, examples like human motion and tire rotation are low-frequency operations (1-100 Hz) and it is impossible to design that low frequency resonant device out of silicon due its high Young modulus. These devices, most remarkable ones are reviewed in Chapter 2, generally have resonance frequencies that are on the order of kHz. Moreover, most of the MEMS devices in literature are designed for single frequency sinusoidal excitation. Nevertheless, the environmental vibrations are generally broadband. Like the applications of our interests, the environment may have impact like excitations with rich harmonic content. Therefore, there is a need for designing low frequency and broadband harvesters, but should still occupy small volume that is at least comparable with the size of a sensor node of figure 1.2.

In this work, FR4, a very well known PCB material, is proposed as an alternative material to design low frequency and broadband electromagnetic (EM) energy harvesters in order to power wireless sensor nodes that are used in human condition monitoring and intelligent tire applications. We propose FR4 for harvesting applications since it generate notable power for a wide range of environmental frequencies with comparable or better performance compared MEMS based devices due to its high intrinsic damping and lower Young' s modulus (about 10 times smaller than that of silicon). FR4 is also low-cost, highly integrable with electronics, and lends itself naturally to electromagnetic sensing as coils can be routed easily on the copper laminates.

Our group has done the pioneering work before in exploring FR4 mechanical properties and its integration with electronics and micro-optics on the same movable platform [5-6]. FR4 is a well-engineered composite material for its electrical, thermal, and mechanical properties and performed very well in reliability tests up to 250 million cycles and can be operated at stress level up to 100MPa and already proved itself to be a good alternative to silicon MEMS devices for certain applications [7].

The FR4 energy scavengers proposed in this study are also well-suited for both low and high-g vibration environments due to the shock stoppers built-in the structure. They are particularly well suited for nearly periodic and non-sinusoidal excitations with rich harmonic content, such as those seen during human running and inside the car tire surfaces.

Chapter 2 investigates the previous energy harvesters with a chronological order to give an insight about what has been done in the literature prior to this work.

Chapter 3 makes the backbone analysis of the governing equations of energy harvesting. First, the reduced model for any inertial device is given. Then, the system responses to sinusoidal and general periodic signals are obtained. For these signals power equations are driven and the optimum conditions for energy harvesting are investigated via base excitation and displacement transmissibility.

Chapter 4 defines the numerical model developed to solve for the coupled equations derived in Chapter 3. First FR4 energy harvester prototype, which is FR4 cantilever system is introduced as a case study to explain the magneto-electro-mechanical model.

Chapter 5 verifies the numerical model with the pulse drive experiments of FR4 cantilever case study, in which the human running is approximated to a pulse excitation. The numerical model results and experiment data are compared while observing the broadband response. In addition, the effects of magnetic damping are investigated experimentally. Then, a new harvester design is introduced and investigated in detail and the scavenged power as a result of experimentally obtained real human hip acceleration data is anticipated via the numerical model.

Chapter 6 first investigates the tire-road contact accelerations. Then, the tire energy harvester design is described. The harvester system with mechanical stoppers is tested by mechanical shaker with real world tire-road contact tangential accelerations as inputs. Later, the power across a load resistance R_L for different vehicle speeds is anticipated for the actual operation. The design is later improved with non-linear FR4 stoppers which withstand the high-g accelerations occurring inside the tire. Contact analysis is performed in Finite Element Modeling (FEM) software, ANSYS.

The thesis is concluded with the summary of the work done and future research work for the FR4 based energy harvesters, especially for tire energy harvesters.

Chapter 2

LITERATURE REVIEW

The history of small scale energy harvesters dates back to 1990s. Especially, the research on MEMS energy harvesters popped out in 1996 under the name of Power MEMS. This new term was first suggested to define a new class of MEMS devices by A.H Epstein, S.D Senturia and their group in MIT [8].

Their target was to establish a MEMS heat engine made out of 1 cm diameter by 3 mm thick Silicon Carbide (SiC) producing power of 10-20 Watt while consuming H_2. It was like miniaturizing large scale gas turbines. The working principle roots to pressurized gas that spins the turbine. The heat that comes from burning the fuel expands air, and the high-speed rush of this hot air spins the turbine.

Later on, this research expended to the vibrational-to-electrical energy harvesters. These devices can be categorized under three types; Electrostatic, Electromagnetic and Piezoelectric power generators. Electrostatic and Electromagnetic generators can be modeled by mass-spring-damper systems since they are inertial devices as it is explained in Chapter 3. To introduce the principle here briefly, the relative vibration of a wound coil and a magnet enables to harvest mechanical energy to electrical energy via Faraday's law of induction. The governing equations and the law of induction is explicated in Chapter 3 in detail.

The electromagnetic power generator model is first proposed in 1998 by Amirtharajah et al [9]. A second order linearized model of the generator is developed by adapting

traditional linear models for loudspeakers. The currents induced in the coil by the vibration in turn generate an electromechanical force that feeds back and damps the mass motion.

In 2000, a power generator is designed to create a minimally sized, economical, and circuit integrated electric power generator capable of producing enough voltage to drive low-power IC or wireless micro sensors where mechanical vibrations are present. This device designed by Neil N. H. et. al. [10] was the first attempt integrating a micro power generator with the wireless module and to a produce enough voltage to drive low-power IC or wireless micro sensors. In addition, the generator consists of five-layer coil manufactured on PCB by the laser-mircomachining. The spring is made out of copper and the magnet is placed on top. The device is able to generate 5μW power when it is excited at its resonance frequency that is 104 Hz with an amplitude of 190 μm. Also, this is the first attempt to integrate an energy harvester into PCB. However, the actuator is made out of copper. In our work, the actuator is made out of FR4, whereas the coil is an external bobbin.

One year later, El Hami et. al. [11] designed and simulated cantilever beam made out of steel. At the tip of the cantilever, a housing is placed. When the system is excited, the magnet mass moves relative to the housing and energy is stored in the mass-beam system. Copper wire is fixed in position between the poles of the magnets three layers each containing 9 single turn solid copper wires. (diameter= 0.2 mm). When the system is vibrated sinusoidally at 320 Hz that is the natural frequency of the device, 1 mW power is obtained. However, the system's disadvantage is being large in volume. In this work, the authors drag attention to the importance of designing low frequency and broadband harvesters for the first time in literature.

In 2002, a commercial IR remote control system is powered with an energy harvester by Neil N. H [12]. As remarkable novelties a zig-zag and a spiral springs are designed, which are then vibrated at different modes (torsion and out of plane) in order to observe the

emf generation. Around 0.8 mW power is obtained across a 1 kΩ load resistance for torsion mode.

In 2004, Kulah H. et al. [13] proposed a device and named this device as frequency-up converter. It has two resonating structures. A big NdFeB permanent magnet is attached to a diaphragm, which is suspended with a soft spring. Thus, the magnet can oscillate at low frequencies. Just beneath this magnet, several silicon cantilevers with different resonant frequencies are placed at an initial distance as second type of resonating structures. There are iron weights on the tip of this array of beams. They also carry the pick-up coil. While the magnet oscillates at low frequency due to environmental vibrations, it catches the cantilevers at a specific point while getting closer to magnetic tips of the cantilevers. Then, it releases the cantilevers while getting away the cantilevers. Due to this catch and release mechanism, the cantilevers start to oscillate at their resonance frequencies until the next catch. During this short time interval, the cantilevers start to oscillate at their mechanical resonance frequency and generate emf. Therefore, the low frequency oscillation of the magnet causes high frequency oscillation of the cantilever. It is like pulling and then releasing the cantilevers. For this reason, the device is called MEMS-based frequency up-converter. However, the practical obtained power levels are at 4 nW

In 2005, a high power EM generator is established by Das S. et al. [14]. The device had a shaft connected to a series of magnets placed on a circular plate. The shaft is rotated with 120.000 rpm via air driven spindle. The magnets rotated with a high rotational speed with respect to stationary coil around. 2.6 Watts of power is obtained. The device is coupled to a transformer and rectifier, delivers 1.1 W of DC electrical power to a resistive load. However, the high rotational speed can not be practically implemented.

In 2006, a linear electromagnetic generator suitable to supply power to body-worn sensor nodes is introduced by Thomas Von Büren et al. [15]. The power production from human motion is optimized. It is characterized by non-sinusoidal waveforms, low

frequencies (below 30 Hz) and large position amplitudes. The spring usage is avoided since designing low frequency structures with silicon is difficult. The magnet makes pure translational motion in a stator. The soft-magnetic spacers between the magnets are used as they act as flux concentrators .Consequently, the generator has a higher flux gradient and thus a higher force capability than designs with only a single magnet.

Most of the harvesters stated here are MEMS based and are optimized for high frequency sinusoidal vibrations. Their resonance frequencies are on the order of kHz. However, environmental vibrations are low frequency and broadband. FR4 with copper laminates is a good alternative material to design low frequency and broadband EM energy harvesters. Moreover, established FR4 based harvesters are suitable to be used for high-g acceleration environments due to developed mechanical stoppers. Furthermore, there is no good numerical model in the literature to be used for optimization. The governing equations and a numerical model are also developed in this thesis.

Chapter 3

GOVERNING EQUATIONS AND MODELING OF AN EM ENERGY HARVESTING SYSTEM

3.1 Introduction to Faraday's law of induction

Faraday's law of induction states that the relative motion between a coil loop and a magnet induces a voltage potential across the coil that is known as Electro Motive Force (EMF). EMF, ε, occurs across the conducting element through the relative motion of magnet due to a magnetic flux, ϕ, change with respect to time. For tightly wounded coils like multirow and multilayer bobbins with N number of turns, this phenomenon is shown as;

$$\varepsilon = -N\frac{d\phi}{dt} \tag{3.1}$$

where ϕ is expressed by the area integral of magnetic flux density, $\vec{B}$,over the bobbin enclosed area, A, that is ;

$$\phi = \int_A \vec{B} d\vec{A} \tag{3.2}$$

Equation 23 can be simplified and combine with equation 24 by assuming A is constant for small displacements and the area vector stays parallel to the magnetic flux direction [16];

$$\varepsilon = -NA\frac{d\vec{B}}{dt} \tag{3.3}$$

3.2 Lenz's Law and Magnetic damping

After Faraday stated the law of induction, Heinrich Lenz has determined its direction and added a minus sign to equation 3.1. He explained the reason as "an induced current is always in such direction as to oppose the motion or change causing it".

This is based on the energy conservation rule. The induced current should create an opposite polarity relative to the time rate of change of the magnetic flux in order to maintain the magnetic flux in the loop area constant. If the polarity of the change and the induced current were on the same direction, they would combine and increase the flux and its time rate of change, thus induce a larger emf at each instant. This would result in infinite induced current, which is a violation of the energy conservation.

Considering that all the designs in this thesis involve moving magnet type harvesters, the current should counter-act the motion of the moving magnet, thus decreasing the kinetic energy of the magnet. This is known as the magnetic damping (counter emf) and it is modeled as a damper in the reduced second order system model that is explained in section 3.3.

3.3 Reduced Second Order Model

The harvesters explained in this thesis have spring-like structure made out of FR4, on which the magnet is attached. Base excitation of the harvester results the vibration of the magnet relative to stationary multirow, multilayer coil causing an induced current. The moving magnet is linked to base with spring-like structure. Like any other inertial devices, the generator can be modeled as a spring- mass-damper system as shown in figure 3.1.

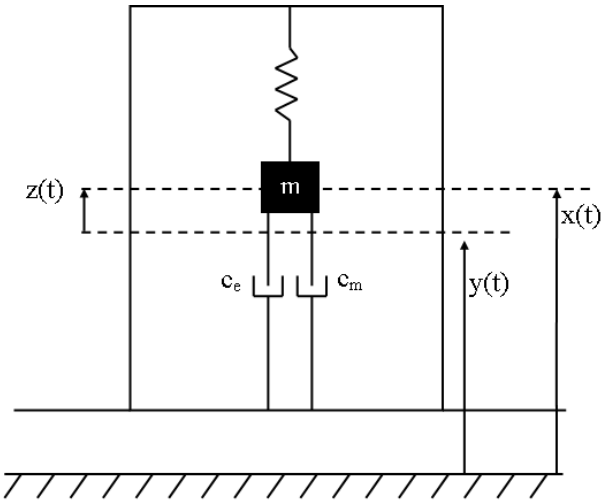

Figure 3.1 Linear mass-spring-damper model for inertial EM generators [17]

The relative displacement of the proof mass, m, with respect to the base, denoted as z(t), can be expressed as the difference of the base displacement relative to the ground, y(t), and the proof mass displacement relative to the ground, x(t):

$$z(t) = x(t) - y(t) \tag{3.4}$$

The equation of motion of the magnet can be expressed as;

$$m\ddot{x}(t) = c\left(\dot{y}(t) - \dot{x}(t)\right) + k(y(t) - x(t)) \tag{3.5}$$

The relative motion, the velocity and the acceleration of the magnet with respect to coil (attached on the base) can be written as;

$$m\ddot{x}(t) = k\left[-z(t)\right] + c\left[-\dot{z}(t)\right] \tag{3.6}$$

Rearranging the equation 3.6;

$$m\left[\left(\ddot{z}(t) + \ddot{y}(t)\right)\right] = -kz(t) - c\dot{z}(t) \tag{3.7}$$

$$m\ddot{z}(t) + c\dot{z}(t) + kz(t) = -m\ddot{y}(t) \tag{3.8}$$

This second order non-homogenous ODE is the governing equation [18]. The total damping, *c*, is the sum of mechanical damping and magnetic damping (counter emf). These are shown as c_m and c_e respectively in figure 3.1.

3.4 Response of the system to Sinusoidal Base excitation

If it is assumed that the input is a pure sinusoid like *y(t)=Ysin(wt),* where *Y* is the input amplitude and ω is the input frequency. Substituting this into the governing equation:

$$m\ddot{z}(t) + c\dot{z}(t) + kz(t) = m\omega^2 Y \sin(\omega t) \tag{3.9}$$

The homogenous solution of this equation gives the transient response, whereas the particular solution gives the steady-state response. If it is considered that time goes to infinity, one can assume a steady state solution such that $z_p(t) = X\sin(\omega t - \theta)$. In order to find the response of the system with the constants X and phase angle, θ, this particular solution is substituted into equation 3.9 and rearranged as [19];

$$X\left[\left(k - m\omega^2\right)\sin(\omega t - \theta) + c\omega\cos(\omega t - \theta)\right] = m\omega^2 Y\sin(\omega t) \tag{3.10}$$

Using the trigonometric relations that are;

$$\sin(\omega t - \theta) = \sin(\omega t)\cos(\theta) - \cos(\omega t)\sin(\theta) \tag{3.11}$$

$$\cos(\omega t - \theta) = \cos(\omega t)\cos(\theta) + \sin(\omega t)\sin(\theta) \tag{3.12}$$

These are substituted in equation 3.10 as;

$$X\left[\left(k - m\omega^2\right)\left(\sin(\omega t)\cos(\theta) - \cos(\omega t)\sin(\theta)\right) + c\omega\left(\cos(\omega t)\cos(\theta) + \sin(\omega t)\sin(\theta)\right)\right] = m\omega^2 Y\sin(\omega t) \tag{3.13}$$

Equating *sin(ωt)* and *cos(ωt)* on both sides of the equation, then

$$X\sin(\omega t)\left[\left(k - m\omega^2\right)\cos(\theta) + c\omega\sin(\theta)\right] = m\omega^2 Y\sin(\omega t) \tag{3.14.a}$$

$$X\cos(\omega t)\left[-\left(k - m\omega^2\right)\sin(\theta) + c\omega\cos(\theta)\right] = 0 \tag{3.14.b}$$

By using eq. 3.14.b, one can find the phase angle as;

$$\left(k - m\omega^2\right)\sin(\theta) = c\omega\cos(\theta)$$

$$\theta = \tan^{-1}\left(\frac{c\omega}{\left(k - m\omega^2\right)}\right) \tag{3.15}$$

By using eq. 3.14.a, magnitude of X can be found such that:

$$X = \frac{m\omega^2 Y}{\left(k - m\omega^2\right)\cos(\theta) + c\omega\sin(\theta)} \tag{3.16}$$

$$|X| = \frac{m\omega^2 Y}{\sqrt{\left(k - m\omega^2\right)^2 + (c\omega)^2}} \tag{3.17}$$

Then, the particular solution (steady-state solution) is found as;

$$z_p(t) = \frac{m\omega^2 Y}{\sqrt{\left(k - m\omega^2\right)^2 + (c\omega)^2}}\sin(\omega t - \theta) \tag{3.18}$$

This is the response of the system to sinusoidal excitations.

3.5 Steady state response and electrical power for sinusoidal inputs

Since the electrical energy extracted from the motion of the magnet slows down the movement of the magnet, electrical energy extraction is modeled as a damper. Then, the mechanical power across the damper is equal to the electrical power extracted that is:

$$P_e = \int_0^{\dot{z}} c_e \dot{z} d\dot{z} = c_e \frac{|\dot{z}|^2}{2} \tag{3.19}$$

The velocity, $\dot{z}(t)$, can be obtained by taking the derivative of equation 3.19;

$$|\dot{z}| = \frac{mY\omega^3}{\sqrt{\left(k - m\omega^2\right)^2 + (wc)^2}} \tag{3.20}$$

Plugging equation 3.20 into equation 3.19;

$$P_e = \frac{\left(c_e/2\right)m^2Y^2\omega^6}{\left(k - m\omega^2\right)^2 + (c\omega)} \tag{3.21}$$

Dividing and multiplying the first term on denominator with m^2 to rearrange such that;

$$P_e = \frac{\left(c_e/2\right) m^2 Y^2 \omega^6}{m^2\left(\frac{k}{m} - \omega^2\right)^2 + (c\omega)} \tag{3.22}$$

$$P_e = \frac{\left(c_e/2\right) m^2 Y^2 \omega^6}{m^2\left(\omega_n^2 - \omega^2\right)^2 + (c\omega)} \tag{3.23}$$

Dividing and multiplying the denominator with w_n^4;

$$P_e = \frac{\left(c_e/2\right) m^2 Y^2 \omega^6}{\omega_n^4\left[m^2\left(1-\left(\frac{\omega}{\omega_n}\right)^2\right)^2 + \left(\left(c_T \frac{\omega}{\omega_n}\right)^2 \frac{1}{\omega_n^2}\right)\right]} \tag{3.24}$$

Making the further re-arrangements;

$$P_e = \frac{\left(\frac{c_e}{2m\omega_n}\right)\frac{m^2}{m} Y^2 \left(\frac{\omega}{\omega_n}\right)^3 \omega^3}{\left[\left(1-\left(\frac{\omega}{\omega_n}\right)^2\right)^2 + \left(\left(\frac{\omega}{\omega_n}\frac{c_t}{\sqrt{km}}\right)^2\right)\right]} \tag{3.25}$$

Where the total damping ratio is

$$\xi_t = \frac{c_t}{2\sqrt{km}} = \frac{c}{2m\omega_n}$$

and the electrical damping ratio can be written as

$$\xi_e = \frac{c_e}{2\sqrt{km}} = \frac{c_e}{2m\omega_n}$$

Plugging these into equation 3.25;

$$P_e = \frac{\xi_e m Y^2 \left(\frac{\omega}{\omega_n}\right)^3 \omega^3}{\left[\left(1-\left(\frac{\omega}{\omega_n}\right)^2\right)^2 + \left(\left(2\xi_t \frac{\omega}{\omega_n}\right)^2\right)\right]} \tag{3.26}$$

This is the generalized form of power extraction from the EM inertial devices. If the EM device is set to work its resonance frequency ($\omega=\omega_n$), the equation simplifies to [20]:

$$P_e = \frac{\xi_e m Y^2 \omega_n^3}{4\xi_t^{\,2}} \tag{3.27}$$

3.6 Steady state response and power for any periodic signal

Like in the cases of human motion and tire-road contacts, the input signals to harvester system may be periodic, but non-sinusoidal. In those cases, Fourier expansion can be used in order to determine the response and generated power of the system. If a signal is periodic with a period of $\tau = 2\pi/\omega_o$, it can be expressed as a summation of harmonically related complex exponentials.

The forcing function that is the right hand side of the governing equation of the system given with the equation 3.9 can be expanded with the alternative Fourier series representation;

$$F(t) = \frac{a_o}{2} + \sum_{n=1}^{\infty} a_n \cos(nwt) + \sum_{n=1}^{\infty} b_n \sin(nwt) \tag{3.28}$$

The Fourier coefficients, a_n and b_n can be calculated as;

$$a_n = \frac{2}{\tau}\int_o^{\tau} F(t)\cos(n\omega t)dt \qquad\qquad n = 0,1,2,3... \tag{3.29.a}$$

$$b_n = \frac{2}{\tau}\int_o^{\tau} F(t)\sin(n\omega t)dt \qquad n = 1,2,3... \tag{3.29.b}$$

Equation 3.28 can be expressed with polar form as;

$$F(t) = \frac{a_o}{2} + \sum_{n=1}^{\infty} C_n \cos(nwt + \varphi_n) \tag{3.30}$$

where $C_n = \sqrt{a_n^2 + b_n^2}$ and $\psi_n = \tan^{-1}(b_n / a_n)$.

Plugging equation 3.30 into equation 3.9, the governing differential equation of the system can be re-expressed as

$$m\ddot{z}(t) + c\dot{z}(t) + kz(t) = \frac{a_o}{2} + \sum_{n=1}^{\infty} C_n \cos(nwt + \varphi_n) \tag{3.31}$$

Equation 3.31 is valid for any periodic signal. In order to find the total response, the superposition method is used. Total response is the summation of individual particular solution individual inputs on the right-hand side of the equation. The sinusoidal functions' response is calculated similar to the analysis in section 3.4. When the response due to DC component is included, the steady state solution of relative displacement of the magnet, z(t), is given as ;

$$z_p(t) = \frac{a_o}{2k} + \sum_{n=1}^{\infty} \frac{(C_n / k)}{\sqrt{\left(1 - n^2 r^2\right)^2 + (2\xi_t rn)^2}} \cos(n\omega t - \gamma_n) \tag{3.32}$$

where $\gamma_n = \theta_n + \psi_n$. ψ_n is a phase angle calculated as $\varphi_n = \tan^{-1}\left(\frac{2\xi_t rn}{1 - n^2 r^2}\right)$ and $r = w / w_n$.

The electrical power can be calculated with the equation 3.19 and the similar method followed with section 3.4. The electrical power for an arbitrary periodic excitation, the general expression for the electrical power is obtained as:

$$P_e = \frac{c_e}{2}\left| -\sum_{n=1}^{\infty} \frac{(n\,w C_n / k)}{\sqrt{\left(1 - n^2 r^2\right)^2 + (2\xi rl)^2}} \sin(n\omega t - \gamma_n) \right|^2 \tag{3.33}$$

This closed-form of electrical power is important and helpful to model the harvester systems numerically that is explained in Chapter 4. If the excitation is sinusoidal, i.e., n=1, equation 3.33 simplifies to equation 3.26.

The magnetic damping coefficient, c_e , in equation 3.38 is given by;

$$c_e = \frac{(\phi)^2}{R_c + R_L + jwL_c} \tag{3.34}$$

This equation can be driven by equating mechanical power to electrical power and is already drived in [21].

3.7 Displacement transmissibility

In Laplace domain, the equation of motion can be represented as;

$$ms^2 Z(s) + csZ(s) + kZ(s) = -ms^2 Y(s) \tag{3.35}$$

The transfer function obtained is;

$$\frac{Z(s)}{Y(s)} = \frac{-ms^2}{ms^2 + cs + k} \tag{3.36}$$

Replacing s=jw; and dividing the equation by *m*,

$$\frac{Z(jw)}{Y(jw)} = \frac{\omega^2}{-\omega^2 + \frac{c}{m}\omega j + \frac{k}{m}} \tag{3.37}$$

Rearranging and dividing the equation by ω_n^2, the magnitude of the transfer function is;

$$T_d = \frac{Z}{Y} = \frac{r^2}{\sqrt{\left(1 - r^2\right)^2 + \left(2r\xi_t\right)^2}} \tag{3.38}$$

This equation is known as displacement transmissibility [19]. The displacement amplitude ratio of the moving mass to base vibration amplitude is optimized when the excitation frequency is equal to the natural frequency. This can be well observed from figure 3.2. When r=1, the displacement transmissibility is maximum. In other words, the base vibration is totally coupled to magnet mass. By this way, the relative motion of the moving magnet relative to bobbin is maximized. This is an important result. The average power equations driven 3.26 and 3.33 gives the maximum power at the mechanical resonance frequency. Due to this phenomenon, the energy harvesters' resonance frequencies are set to excitation frequency if the excitation is sinusoidal.

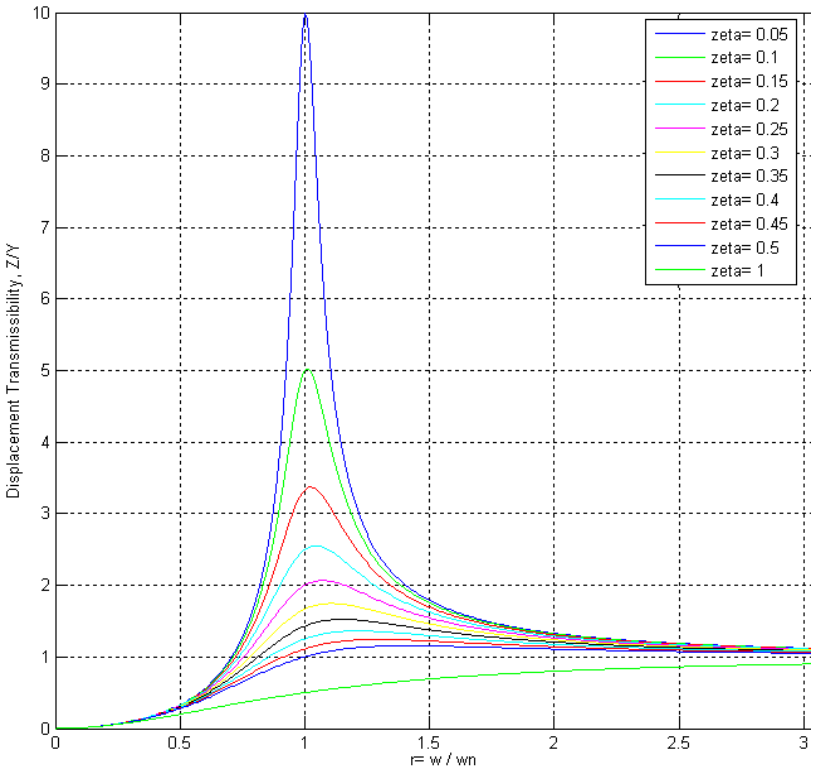

Figure 3.2 The Displacement Transmissibility curve for different ξ values.

3.8 Normalized Power Density (NPD)

One of the main aims of the energy harvesters is to be compact while generating electricity. Therefore, the device performance is generally stated with a power density (W / m^3) in the literature. However, the testing conditions of stated harvesters are very different (i.e acceleration amplitudes, frequency). For resonant harvesters, which are the devices tested only with sinusoidal input at their mechanical resonance frequency, S. P. Beeby et al. [20] proposed Normalized Power Density (NPD) in order to compare the performance of different stated generators with each other. The amplitude of the peak acceleration of the base, A_p, is given by $A_p = \omega^2 Y$. Moreover, damping factor, c, is related to the total damping ratio, ξ_T, by $c = 2m\omega_n\xi_T$, equation 3.29 can be restated as:

$$P_e = \frac{(mA_p)^2}{2c} \tag{3.39}$$

The average electrical power is proportional to A_p^2. Since the testing frequency is resonance frequency, S P Beeby normalized the power of stated harvesters only with acceleration square, A_p^2. Then, the formulation of NPD is given as;

$$NPD = \frac{P_e}{{A_p}^2 V} \tag{3.40}$$

where V is the volume in m^3. The NPD is therefore has the unit of "kgs / m^3". NPD will be used as a tool in Chapter 4 to compare our harvesters with the other harvesters.

Chapter 4

MAGNETO-ELECTRO-MECHANICAL NUMERICAL MODEL

4.1 Introduction

In Chapter 3, analytical equations are derived for the steady state response of the moving magnet's relative motion with respect to the base including the electrical power calculations for sinusoidal inputs as well as any periodic function. These equations are helpful to understand the EM harvester system. However, there is a need of a good use of these equations in a simulation environment to do numerical analysis.

In this chapter, the total physical harvester system with all coupled energy domains is modeled in MATLAB / Simulink including the open loop (without) and closed loop (with magnetic damping) operations. For the magnetic domain calculations, the magnet and its magnetic flux density are modeled in COMSOL / Multiphysics module. The performance of this magneto-electro-mechanical model is verified with simple shaker experiments.

4.2 Coupled Energy Domains

The ambient vibrations cause the base and thus the magnet to oscillate. The relative displacement of the magnet with respect to stationary coil causes a magnetic flux change with respect to time. This change induces voltage (emf) in pick-up coil. However, induced current in the coil damps back the mechanical motion of moving magnet. Hence, the total

physical system consists of three coupled-energy domains, which are mechanical, magnetic and electrical as shown as in figure 4.1

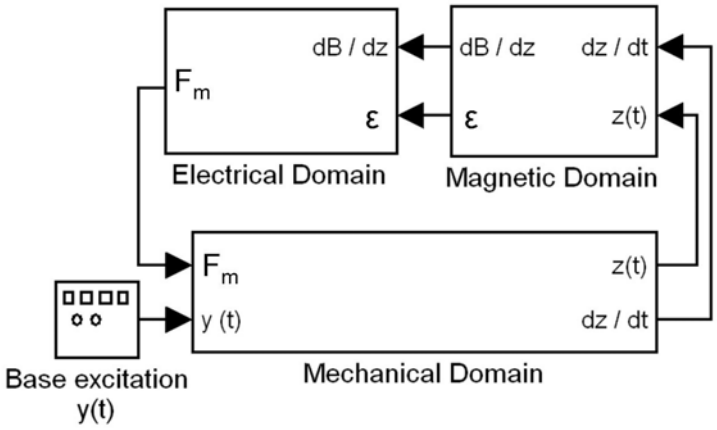

Figure 4.8 Coupled Energy Domains

4.3 Governing equations, EMF and Magnetic Damping revisited

In this sub-section, some of the governing equations of section 3 are summarized and extended since the numerical model that is explained in the next section solves for these equations respectively.

The governing differential equation of the relative motion of the magnet , z(t) , is given by equation 3.11. As already reviewed in section 3.1, the electrical energy is generated based on Faraday's law of electromagnetic induction stating that the time rate of change of magnetic flux (ϕ) through a coil having *N* number of turns induces a voltage (emf) given by equation 3.1. This equation is simplified by assuming *A* is constant for small displacements and the area vector stays parallel to the magnetic flux direction. Since $\vec{B}$ is a function of relative displacement, and the relative displacement is a function of time, equation 3.3 is rearranged by using the chain rule as;

$$\varepsilon = -NA\frac{dB}{dz}\frac{dz}{dt} = -NA\frac{dB}{dz}\dot{z}(t) \tag{4.1}$$

If the pick-up coil terminals are left open (i.e, open-loop operation), then the above expression is enough itself to calculate ε. If an induced current is generated by the presence of a load such as a capacitor or a battery to store the energy, then the system is in closed-loop mode and there is an additional magnetic damping term generated by the induced current i(t), which effectively counter-acts the motion of the magnet as it is discussed in Section 3.2. This magnetic damping force (F_M) dissipating the kinetic energy of the vibrating magnet can be expressed as [22];

$$F_M = NA\frac{dB}{dz}i(t) \tag{4.2}$$

This damping force should be considered while establishing the model since it plays an important role in EMF generation limitations. Its effect is investigated in Chapter 5 in detail

4.4 MATLAB / Simulink Model

Equations 3.11, 4.1 and 4.2 are used to build the numerical model in MATLAB / Simulink environment. The explicit model is shown in **Figure 4.1**.

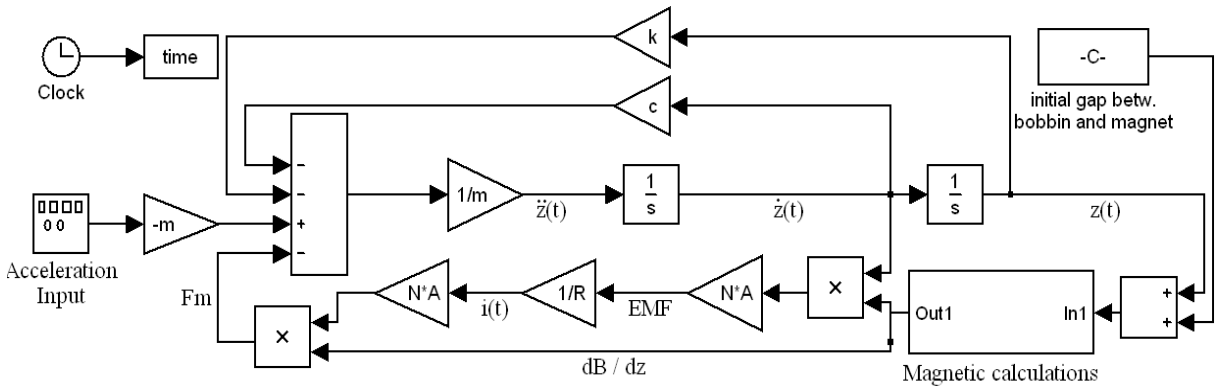

Figure 4.9 Closed Loop Model

When the system operates on open loop, there is no magnetic damping since there is no current circulating due to open terminals of the coil. There is still emf generated, but there is no counter emf. When this is the case, the F_M connector line is disconnected as shown in **Figure 4.2**. In other words, electrical damping, c_e ,does not occur.

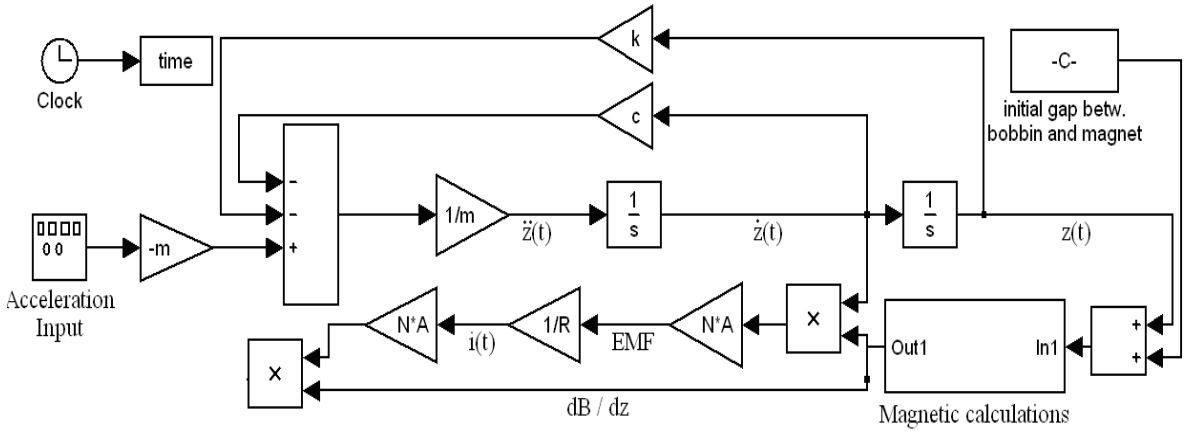

Figure 4.10 Open Loop Model

The basic advantage of this numerical model is all types of ambient acceleration inputs (i.e human running and road-tire contact) can be given to the system in order to predict EMF and magnetic damping effects. Thus, evaluation of the system performance and optimization can be easily executed for any energy harvester including MEMS based and FR4 based devices once the critical parameters are known.

The verification of the numerical model is overviewed in section 4.6 and the magnetic calculations subsystem, which involve magnetic modeling is explained in section 4.7.

4.5 FR4 cantilevers

Before reviewing the magnetic modeling over FR4 cantilever case study, a short introduction is given in this section. In order to test the FR4 performance as a vibrating platform and verify the numerical model, different types of cantilever beams as shown in

figure 4.4 are cut from copper laminated FR4 sheets having thicknesses ranging from 178 μm to 320 μm.. For cutting process, a PCB cutting machine that is already available in Optical MEMS Laboratory (OML) facilities is used.

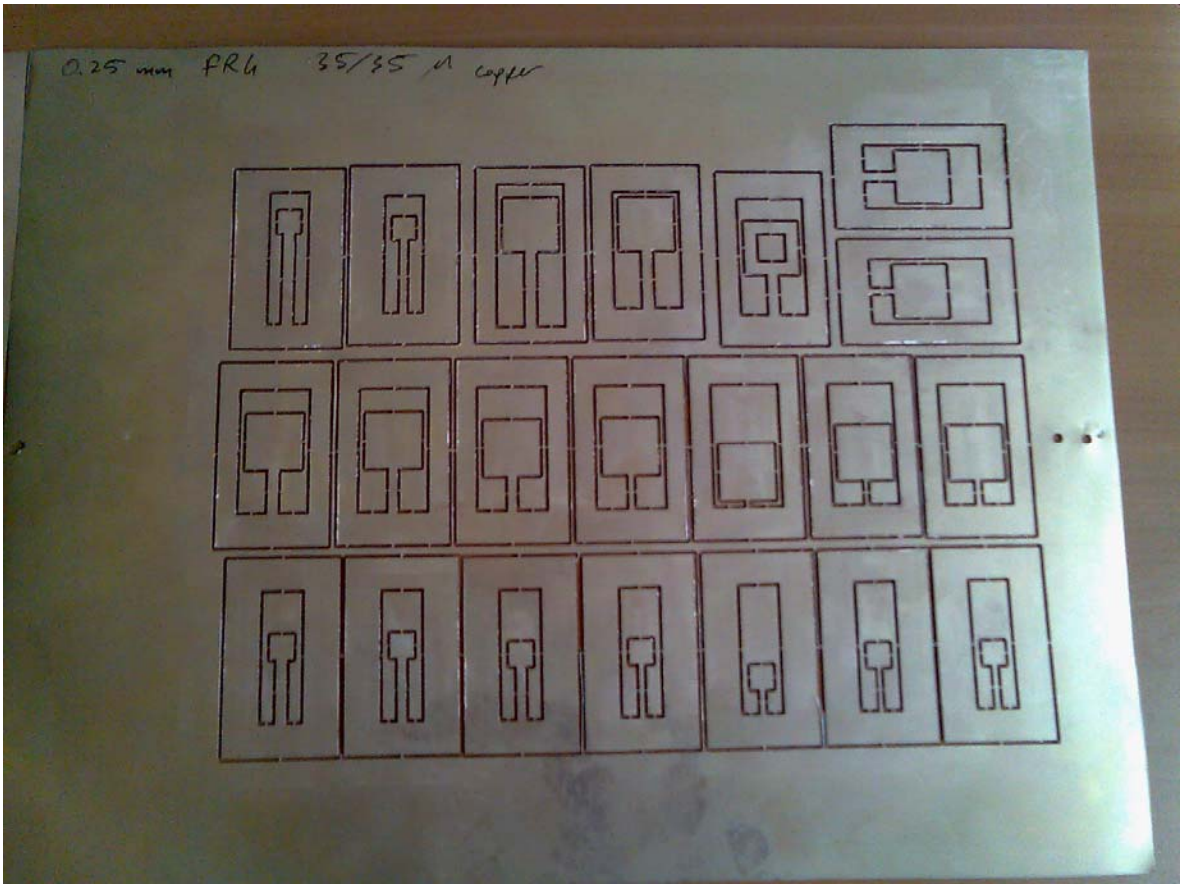

Figure 4.4 320 microns thick FR4 plate from which different types of cantilevers are manufactured

Cantilevers that are spring-like structures with high intrinsic damping have square pads at the end on which the magnet could be attached. Despite these pads, the structures shown in figure 4.4 can be still approximated as cantilever beams with uniform width. In order to

calculate the natural frequency of the beams , f , the following equation that is derived by Timoshenko is used [23];

$$f = \frac{1.732}{2\pi}\sqrt{\frac{EI}{ml^3}} \tag{4.3}$$

The resonance frequency depends on width, thickness and length of the cantilevers. Therefore, different cantilevers having various width, length and thicknesses are manufactured. Since the environmental vibrations are between 0-100 Hz, the resonance frequency is aimed to be lowered as much as possible without any failure. In order to achieve low-frequency harvester, either the spring constant is lowered or the magnet mass is increased.

4.6 FR4 Cantilever Case Study

One of these cantilevers is selected as a case study to explain the magnetic modeling process over the cantilever system and also to test the numerical model (Chapter 5). Figure 4.5.a through 4.5.c demonstrates the preliminary energy harvester design, whose parameters are listed in table 1.

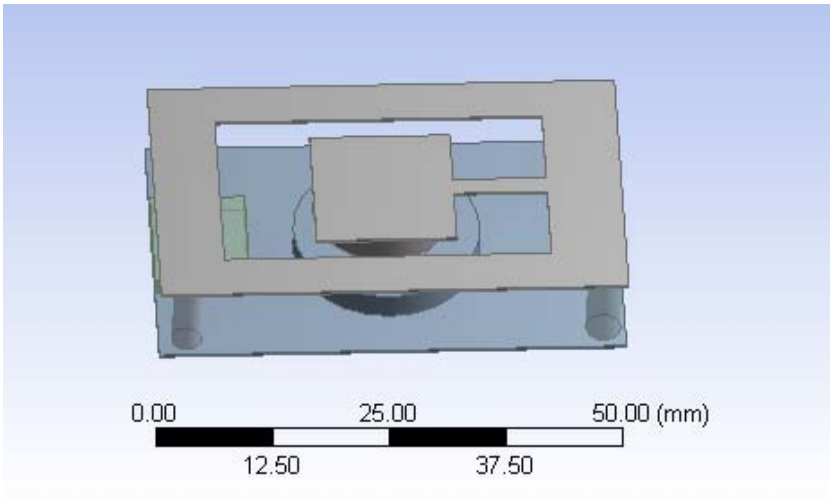

(a)

(b)

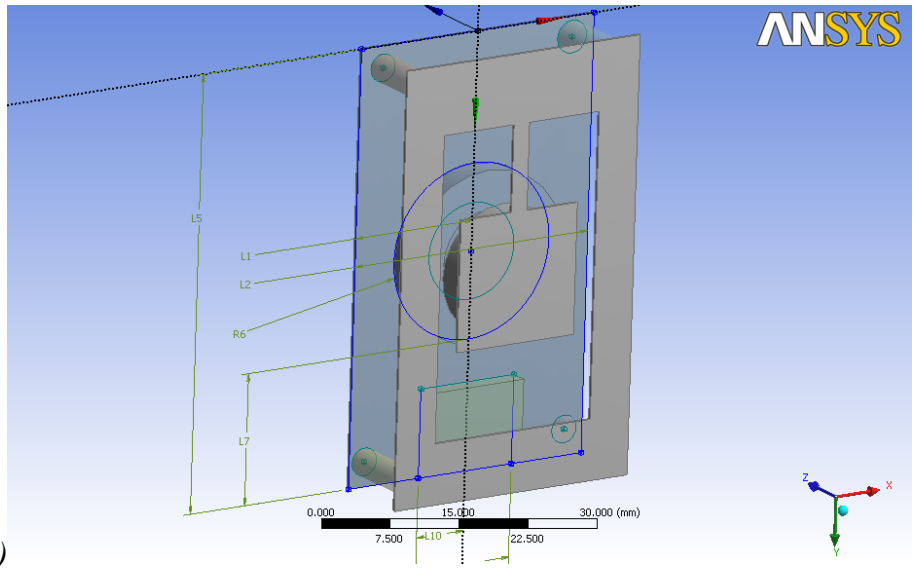

(c)

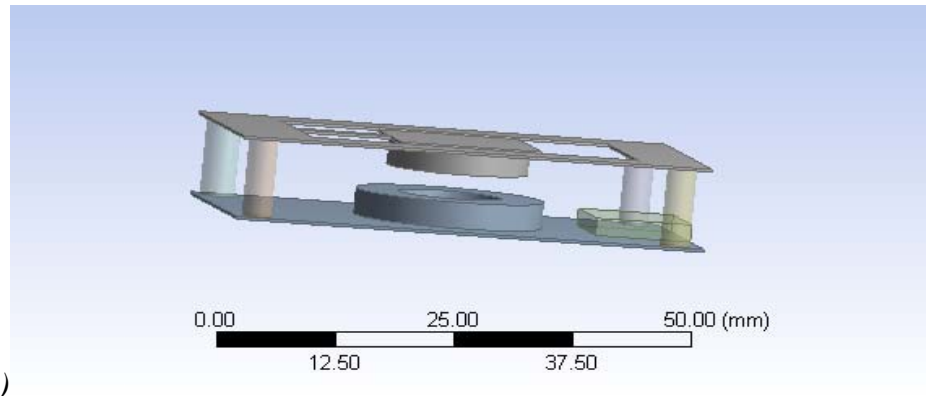

Figure 4.5.a b c The preliminary FR4 cantilever design. The lower plate on which the bobbin is placed is also copper laminated FR4.

Table 4.1 FR4 cantilever case study and magnetic model parameters

Parameter	Value
f_n	24,8 Hz
k	98 N / m
Q	23,36
l_b	10 mm
w_p	15 mm
t	0.32 mm
Nd	NdFeB
Grade	N35
B_R	0,98 T
m	4.036 gr
B_r	1 Tesla
R	7,72 mm
H	3.17 mm
r_{ci}	7,5 mm
r_{co}	12,2 mm
L_c	15.56 uH
N	741
R_c	100 Ω
R_L	100 Ω

The magnet is attached on the square pad that is at the end of the cantilever. On the lower platform, multilayer coil with N turns coated with Parylene is placed. It is located just beneath the magnet, which is free to vibrate due to ambient vibrations.

4.7. Magnetic modeling

Since the only unknown parameter in equations 4.1 and 4.2 is the position rate of change of the magnetic flux density, dB/dz, a mathematical expression is needed to

express this parameter. Therefore, the magnet should be modeled precisely. The FR4 cantilever beam and the *Nd* magnet, whose parameters are listed in table 4.1, are chosen to exhibit the procedure for obtaining mathematical expression.

The bobbin used in this work is cylindrical air-core, multirow and multilayer coil and therefore using a cylindrical magnet is reasonable. For a cylindrical magnet (figure4.6) having a diameter of 2R and a height of H, the magnetic flux density on the axis line at a distance z from the pole surface is defined with the equation 16 [24].

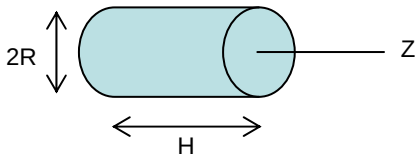

Figure 4.6: The cylindrical magnet

$$B = \frac{B_r}{2}\left(\frac{(H+z)}{\sqrt{R^2+(H+z)^2}} - \frac{z}{\sqrt{R^2+z^2}}\right) \tag{4.4}$$

By using teslameter (Magnet-Physik F54 model), the variation of B is determined as a function of z is determined experimentally. The transverse Hall probe is aligned exactly with the pole axis and the probe that is attached to a micrometer stage is held fixed at that position (z=0). The probe is then driven away from the pole position with 250 microns increments along the axis of the centerline within the help of the micrometer stage. Figure 4.7 shows the magnetic flux density as a function of z. Actually, the magnet's magnetic lines are like a fountain when considered in 3D. However, the magnetic flux change along the centerline is critical for modeling purposes in COMSOL.

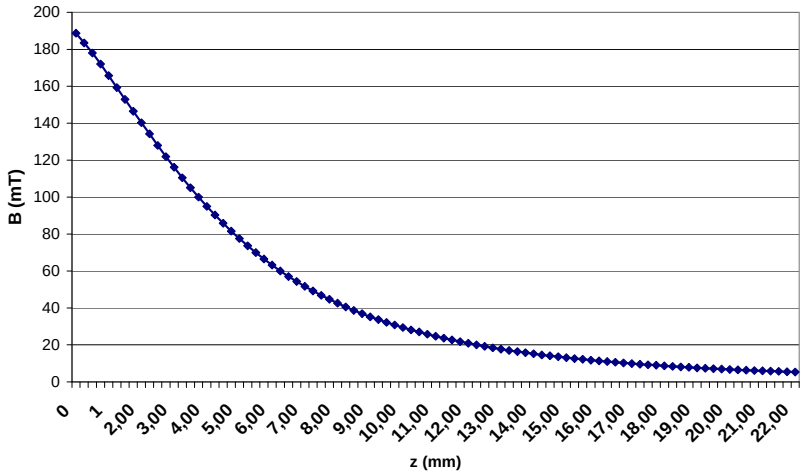

Figure 4.7 Experimentally obtained magnetic flux density of the test case magnet along its axis of centerline.

In COMSOL Multiphysics module, 2D axis-symmetric magnetostatic analysis of the magnet is performed. Using the centerline distribution, the magnetization of the magnet is approximated to analytical and experimental values. While modeling the single magnet, the 2D axissymmetry is preferred since the magnet has cylindrical shape. Around the magnet, the air is modeled, whose μ_r is 1. After fine meshing and solution of the domain, the magnetic flux density distribution is obtained as shown in figure 4.8.

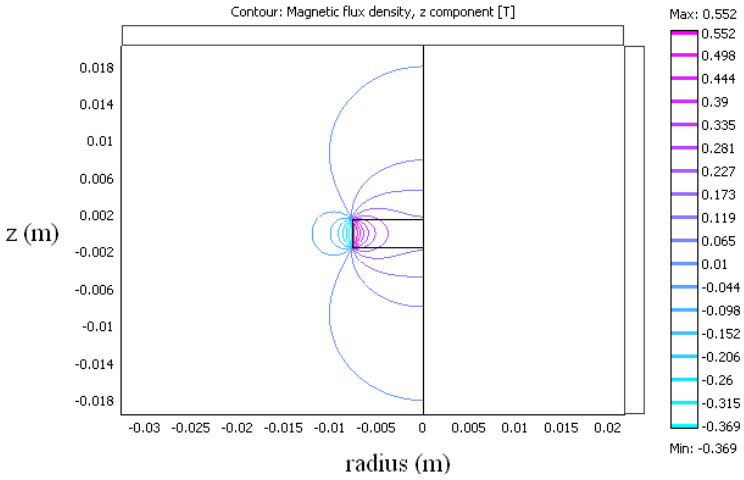

Figure 4.8 2D axis symmetric flux lines of the magnet used in FR4 case study.

First, the magnetic flux density over the magnet's centerline is obtained in order to compare the analytical, experimental and simulation results. As shown in figure 4.9, the experiments obtained by teslameter testing and analytical modeling of the magnet given with the equation 4.4, fits well with the COMSOL simulation modeling.

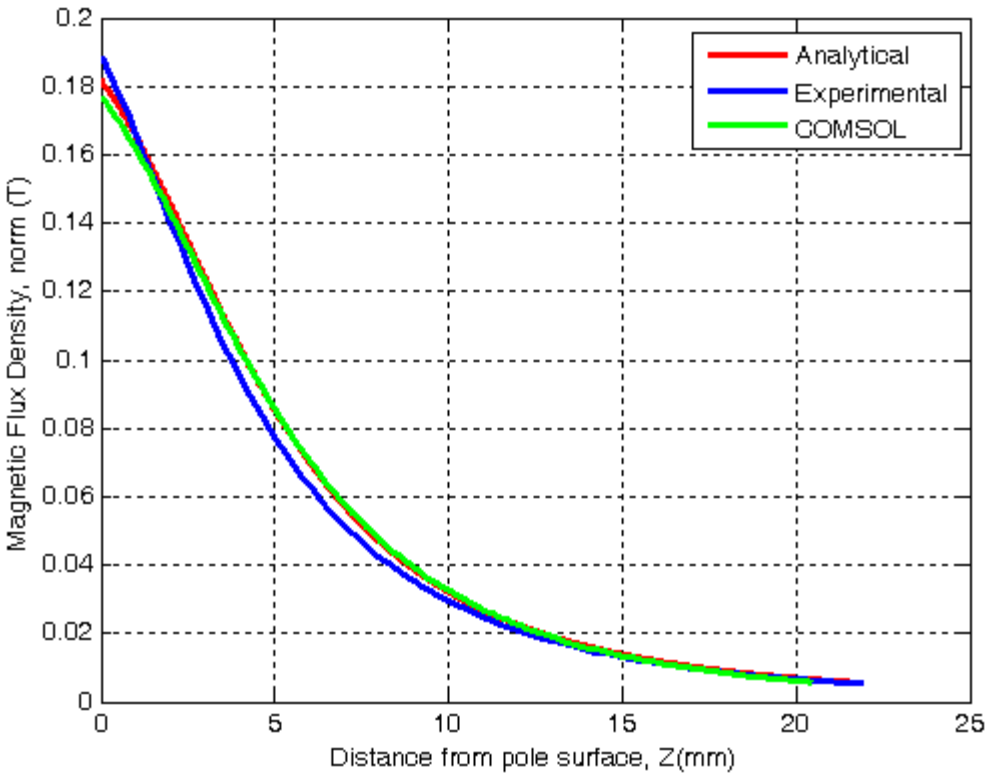

Figure 4.9 Comparison of Magnetic flux density along the axis of magnet centerline.

After modeling the magnet in COMSOL, the average magnetic flux density of the magnet over the bobbin area is determined. As given in equations 4.1 and 4.2, the important criterion is to know *B(z)* over the enclosed area, *A*. This is shown in figure 4.10 in more detail.

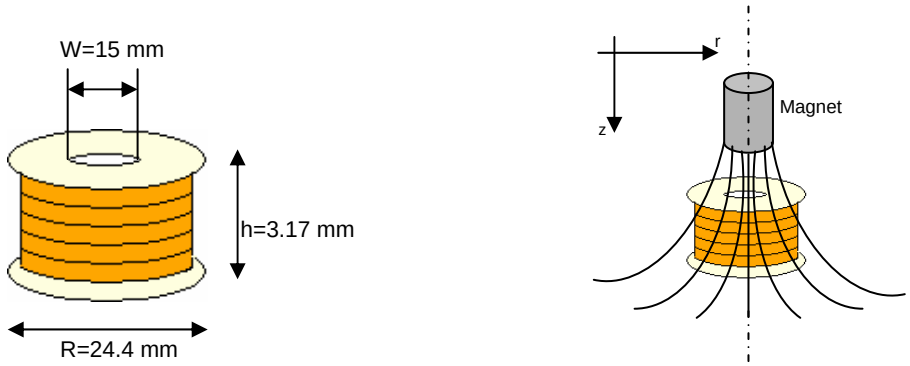

Figure 4.10: a)Bobbin used in experiments b) Magnetic flux lines over bobbin area

By using small increments of z values, much more precise magnetic flux density values are extracted from COMSOL over *A* as shown in figure 10.b. The radial flux components are not taken into consideration since their projection to flux area does not create any flux density.

In Figure 4.11, the graph of magnetic flux density z component as a function of z over bobbin diameter A is shown for different distances that are from magnet pole to the bobbin center. As the distance between the magnet and the bobbin increases, the magnetic flux density decreases sharply.

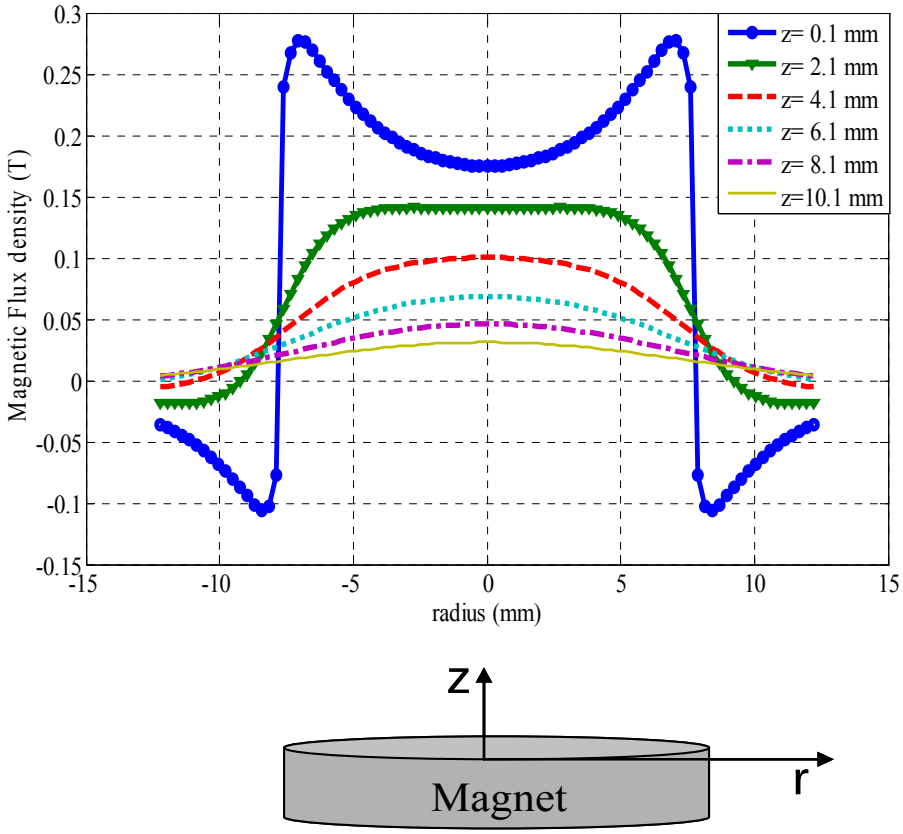

Figure 4.11. Magnetic flux density z component over the pick-up coil (Table 1) enclosed area at various z distances from the magnet pole surface

The figures 4.9 and 4.11 are similar graphs. However, figure 4.9 shows only B values as a function of z along the axis of the magnet, whereas figure 4.11 shows B values as a function of z over *A*. For each z value, B is averaged to a single value for those specific distances. Finally, averaged magnetic flux density z component values as a function of distances that are from magnet pole to bobbin center are obtained.

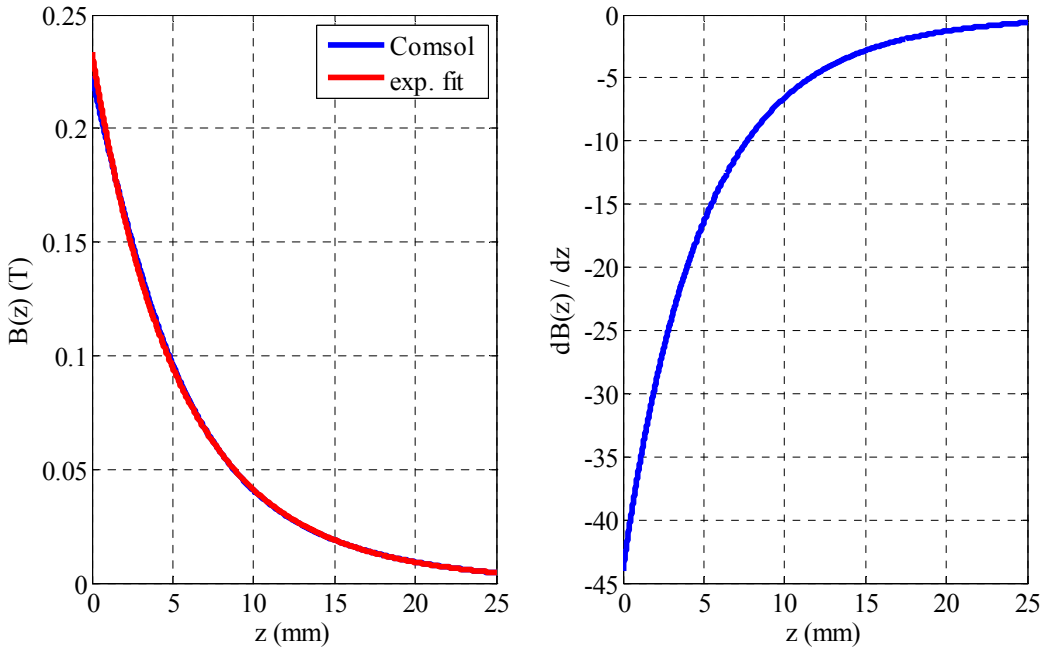

Figure 4.12 (a) Average magnetic flux density distribution (B(z)) over the bobbin area versus distance from the magnet pole surface, z. The function is extracted from COMSOL by the data obtained from experiments. The exponential fit is done to express this function mathematically in MATLAB/ Simulink model. (b) Position rate of change of magnetic flux density, dB/dz versus distance from the magnet pole surface, z.

As it is emphasized before, the only unknown parameter to calculate ε in simulations is dB/dz. To fit a mathematical expression defining the behavior shown in figure 4.12.a , least square method is used. A third order exponential fit is performed for defining B as a function of z:

$$B(z) = e^{Az^3+Bz^2+Cz+D} \tag{19}$$

Now, the derivative of equation 19 can be easily calculated as;

$$\frac{dB(z)}{dz} = \left(Az^2 + Bz + C\right)e^{Az^3+Bz^2+Cz+D} \tag{20}$$

Finally, the B (z) and ϕ distribution is obtained with a fine magnetic modeling via COMSOL. Once B (z) is expressed with a third order exponential fit, its derivate can be easily implemented into simulink in oder to solve the equations needed to calculate emf.

4.8 Implementation of magnetic modeling

The mechanical domain outputs of z(t), and $\dot{z}(t)$ of the moving mass, are taken as inputs in magnetic domain in order to calculate emf (see figure 4.2).

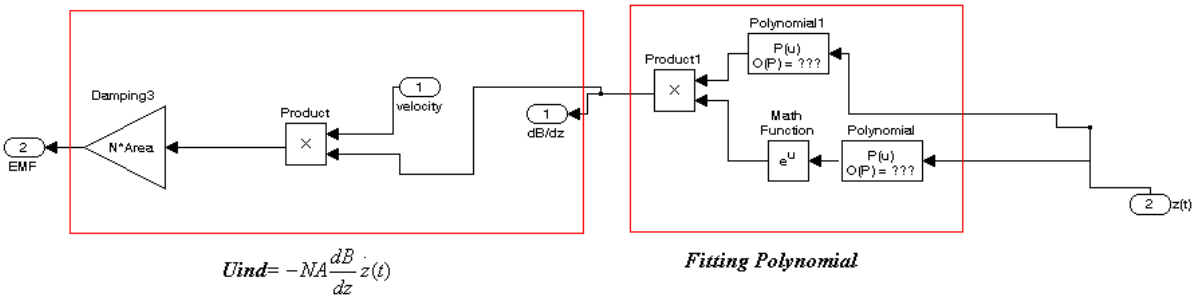

Figure 4.13: The magnetic subsystem is explicitly shown.

Since the bobbin has a thickness in z direction, dB/dz is calculated along the height of the bobbin and it is also averaged along its thickness, h. In magnetic calculations subsystem, the fitting polynomial is calculated for many times along h. Once dB/dz is multiplied by velocity and then N and A, the emf is obtained. If the system is in closed loop operation, magnetic damping is calculated additionally as calculation methodology is shown in figure 4.13.

Chapter 5

NUMERICAL MODEL VERIFICATION AND HAVESTER DESIGN FOR HUMAN RUNNING

5.1 Introduction

In the previous chapter, a numerical model of an EM harvester system is established using MATLAB / Simulink and COMSOL. This model is helpful to simulate the system parameters for various types of inputs. One of these inputs is human running. As it is indicated before, human running motion is one of our application interests. First, it is a low frequency motion. Second, there are several types of wireless sensors that are implantable or body-worn. Third, several portable electronics are carried on the body and the body is a source of environmental vibration. Especially, considerable amplitudes of acceleration may occur while running.

In this chapter, the numerical model introduced in Chapter 4 is verified for sinusoidal resonance excitation as well as for pulse excitation with the shaker experiments. Considering each stride as an impulse to the harvester system, the running motion is approximated with pulse excitation first. Meanwhile, the harvester system is tested with closed loop and open loop operations. Thus, the effects of magnetic damping are investigated clearly. Later, the real acceleration data is collected from human subjects experimentally. Then, the model prediction of the power generated is simulated for FR4 cantilever of figure 4.5 with these signals. In the light of the experiments, a new harvester

design is developed. With this design, the power generation is increased while the volume of the device is decreased compared to FR4 cantilever.

5.2 Pulse Drive of the FR4 cantilever

During the human motion, each stride is like an impulse to the body. Even the legs can be modeled as spring mass damper systems [25]. If the harvester unit that is FR4 cantilever of figure 4.5 is placed on the hip area, the magnet will oscillate relative to stationary coil since the body is vibrated due to this stride impulse. Therefore, the body acts like the base and the stride impulse causes base excitation. This environmental vibration source may be harvested into useful electrical energy with FR4 cantilever. Before working with the experimentally obtained hip area accelerations, the stride is approximated to a pulse input. By this way, the numerical model can be also tested easily.

Average human walking and running stride frequency may vary between 1-4 Hz, where the average is 2.75 Hz [25]. During the average running, the acceleration amplitudes are around 15 m/s^2. Also, the stride contact time to ground is 50% of the period. From Chapter 3 results, it is concluded from equations 3.30 and 3.43 that the optimum electrical energy occurs at the resonance frequency. However, it is difficult to design a resonator at these low frequencies. Nevertheless, electrical energy can be still obtained at off-resonance operation. Since the excitation is impulse, the power generation will be optimized at harmonics.

In order to observe energy generation at harmonics and to test the numerical model verification, a frequency sweep is performed by using a mechanical shaker (Model: Data Physik). Figure 5.1 shows the schematic experimental setup.

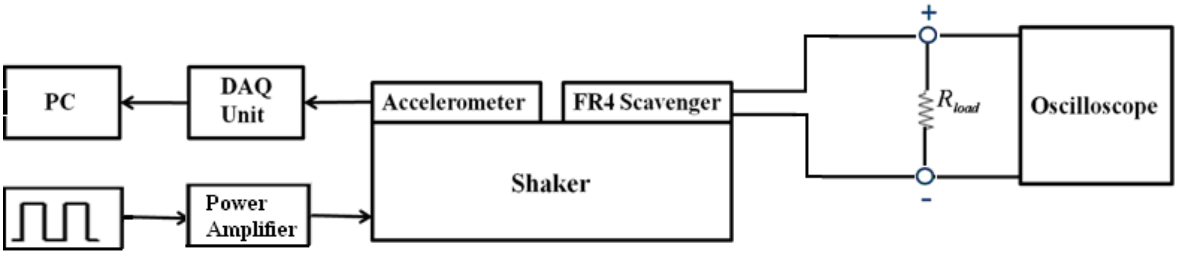

Figure 5.1 Mechanical Shaker experimental setup

The desired signals are fed into the power amplifier, which amplifies the signal to shaker and causes the shaker to supply the desired vibrations at desired amplitudes. However, the shaker should be driven by displacement data. Therefore, the integral of the acceleration data should be taken twice and this should be fed into the shaker in order to obtain desired acceleration waveforms. Figure 5.1 demonstrates the experimental setup for closed loop operation. During the experiments, the RMS voltage across R_L is monitored for both open and closed loop operation. Figure 5.2 demonstrates the shaker on which accelerometer and a dummy FR4 sample is placed.

Figure 5.2 The mechanical shaker

The frequency sweep of FR4 cantilever with an acceleration amplitude of 15 m/s2 having 50% duty is performed and the obtained data is demonstrated in figure 5.3

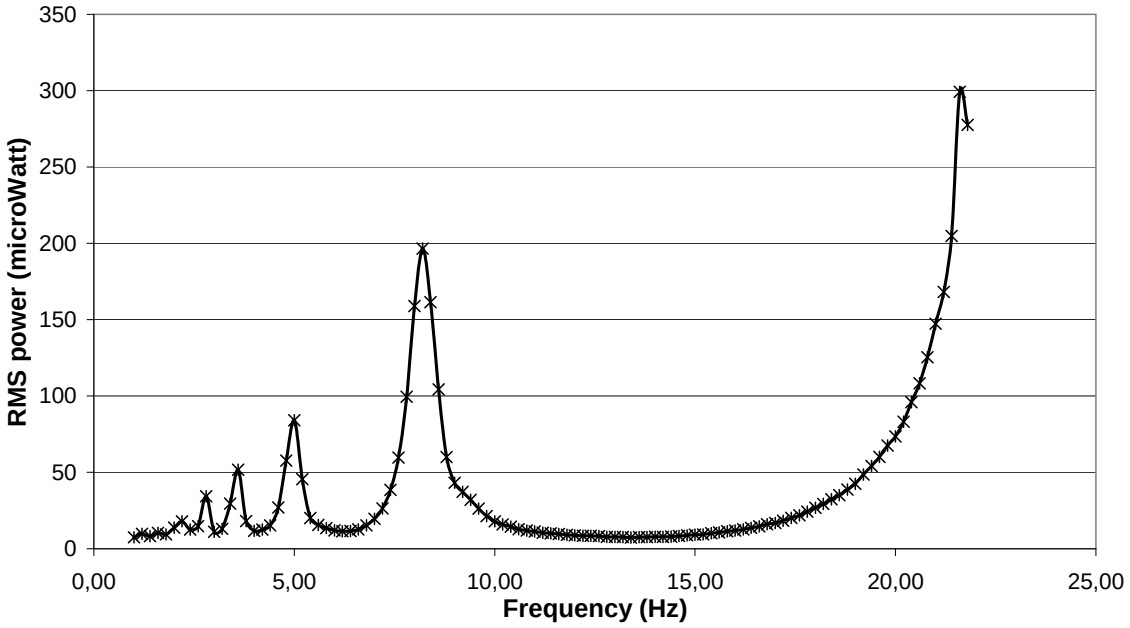

Figure 5.3 The frequency sweep of FR4 cantilever with pulse input

The FR4 cantilever having a resonance , f_n , of 24.8 Hz has failed mechanically closer to its resonance frequency. However, figure 5.3 shows the harmonics and obtained power. Notice that each peak is fairly broad. The maximum RMS power would be obtained at the resonance frequency. Nevertheless, there are local peaks at odd harmonics of f_n (i.e., f_n, $f_n/3$, $f_n/5$ etc.) since square wave does not have even harmonics. When the input acceleration harmonics coincide FR4 cantilever's harmonics, the local peaks are observed. This is the experimental validation of the Fourier series expansion of a general periodic function, where the signal can be defined as the sum of harmonically related exponentials (see Chapter 3, section 3.5). It is also very important to remark that mechanical oscillations

are always at f_n even the input frequency is different from f_n. An oscilloscope screen shot, which is shown in figure 5.4, demonstrates the induced emf waveform and the input acceleration waveform. Notice that the frequency of the oscillation is at f_n even if the excitation pulse is at 5 Hz.

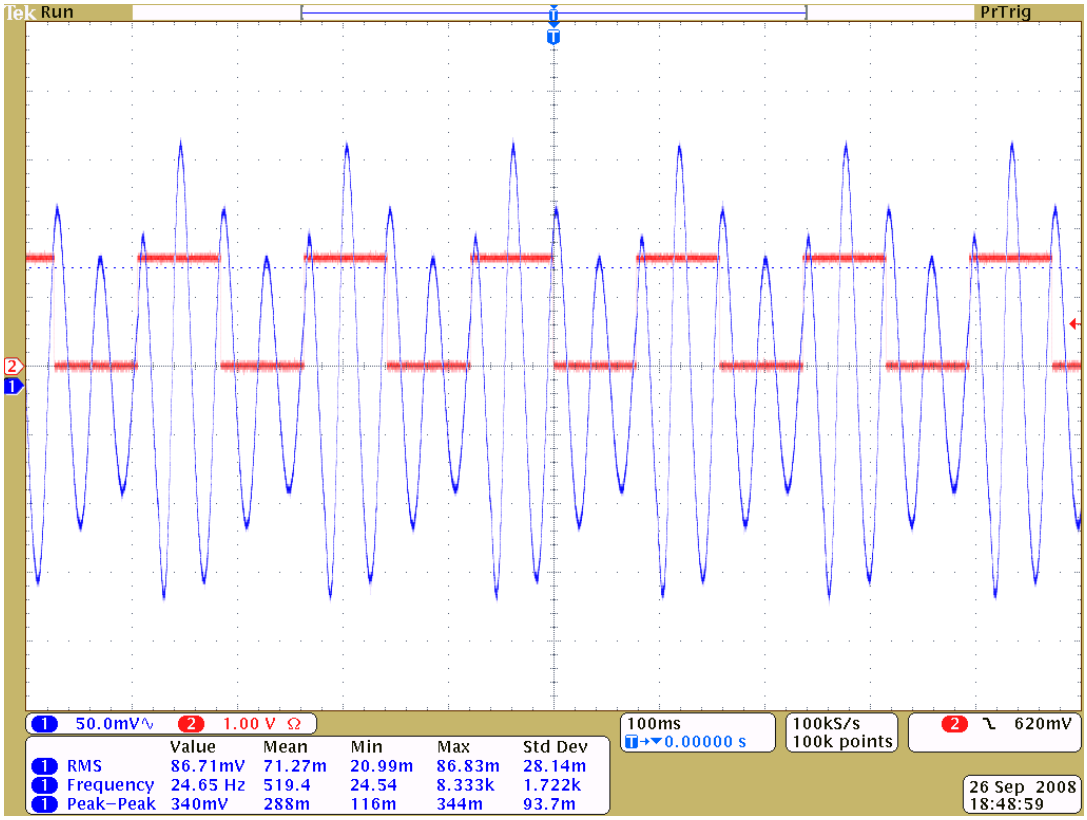

Figure 5.4 Signal 2 (Red) is input whereas the signal 1 (blue) is the induced emf across R_L. Note that the oscillations are always at f_n.

The human motion frequency range is 1-4 Hz. Figure 5.5 shows the low-frequency human motion range. Note that there is a local power peak close to the average human running frequency that is 2.75 Hz. It is the $1/7^{th}$ harmonic. Despite off-resonance operation which already decreases power generation efficiency. This kind of energy generation at

harmonics is very important to design broadband harvesters, which is one of the main aims of this thesis. FR4 is ideal material for designing these broadband devices since it has a lower *Q* value when compared to silicon-based devices, which have high *Q* values. As this is already a good example, the environmental vibrations are broadband besides being low-frequency. This kind of energy generation at harmonics will lead us to design broadband and compact harvesters for wireless tire sensors, which is investigated in Chapter 6 in detail.

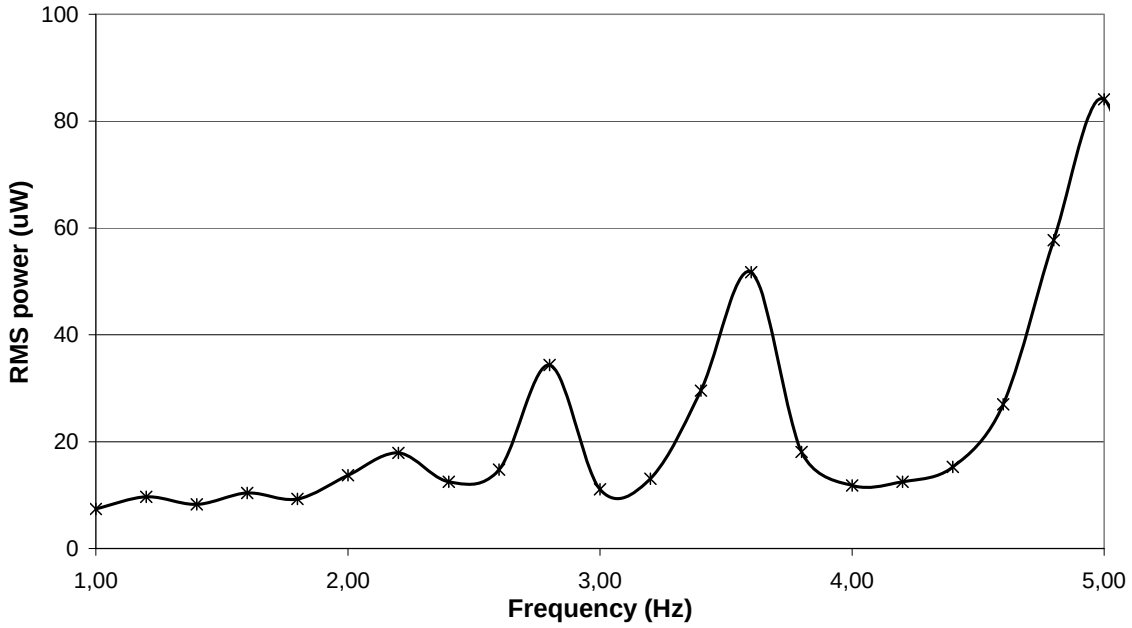

Figure 5.5 Experimental EMF generation of FR4 cantilever system to pulse input at human motion frequency range

Approximating every stride impulse crudely to pulse excitation having 15 m/s^2 amplitude and 50% duty, the performance of FR4 cantilever could be observed. When the excitation frequency is close to *fn*, the power levels are satisfying (see figure 5.3). However, the power levels decrease sharply at human motion frequency range.

5.3 Magnetic damping effects

Besides testing the performance of FR4 cantilever, the pulse drive experiment is also used to observe the effects of magnetic damping. As it is already reviewed sections 3.2 and 4.3, the counter emf reduces the magnet's kinetic energy and slows down the magnet, limiting the induced emf that could be generated.

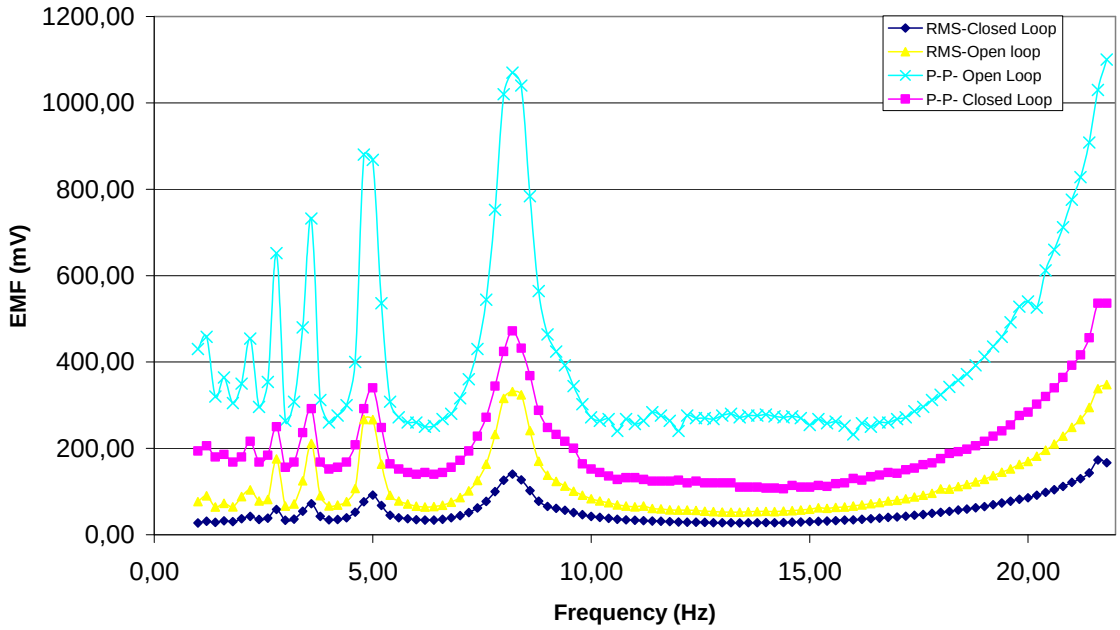

Figure 5.6 Experimentally observed effects of magnetic damping Again the experiment is cut at that specific frequency due to failure of FR4 cantilever

This effect is clearly observed during the experiment. Figure 5.6 clearly demonstrates the effects of magnetic damping. As it is observed from the figure, p-p and RMS induced voltage values differs for closed loop (with magnetic damping) and open loop (without magnetic damping) cases for the same pulse input. At closed loop, the emf is measured across R_L whereas; open loop operation voltages are measured at the open coil terminals.

For this pulse drive experiment, the open loop potential is nearly 3 times larger than the closed loop potential since there is no current circulating in the bobbin to damp out magnet's motion. On the other hand, the induced emf decreases due to circulating current when the coil terminals are closed via R_L.

5.4 Numerical Model Verification

As it is indicated before, the pulse drive experiment is also performed to test the numerical model. FR4 cantilever EM harvester system that is already modeled in Simulink is simulated with the exact pulse input emphasized in section 5.2. The system parameters are given in table 4.1. Figure 5.7 shows below the comparison of numerical model results with the experimental results.

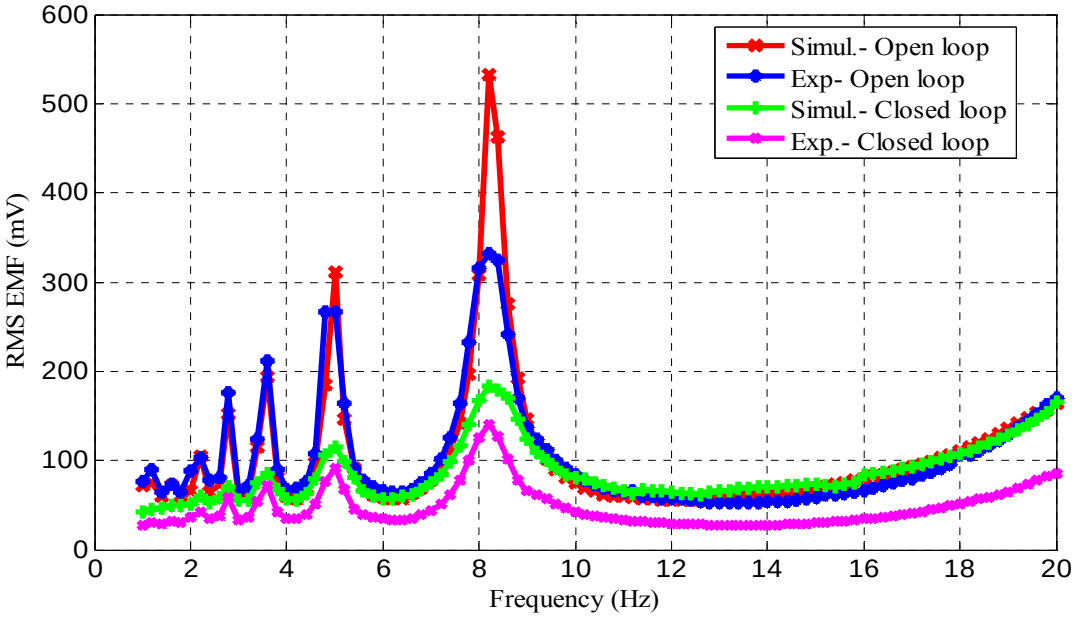

Figure 5.7 Frequency sweep results only showing the harmonics with pulse acceleration input using the FR4 cantilever. Both simulation and experimental results are showing for both open-loop and closed-loop cases.

Despite the large number of variants in mechanics and magnetics, the numerical model that is explained in previous chapter agrees well with the experiments for both open-loop and closed-loop cases. This verified simulation technique is valuable in anticipating the induced voltage for EM harvesting systems. It also solves for the magnetic damping precisely.

5.5 Human Hip Acceleration Data

Human running motion is investigated as an exemplary body motion After the FR4 cantilever is tested and the numerical model validated for this EM harvesting system, the human acceleration waveforms are obtained experimentally in order to be used for numerical model. An accelerometer is placed on the hip area of 3 human subjects, where all are male and do not have any health problems. The subjects have an age average of 25.3 and a weight average of 67.6 kg. Before performing the experiments, subjects consent to participate in the experiments voluntarily.

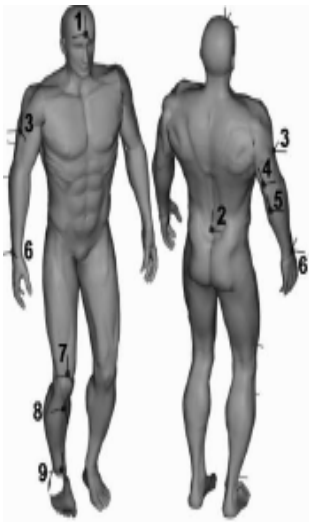

Figure 5.8 Possible wireless sensor placement points [22]

The available and possible points for sensors placement on the human body are shown in figure 5.8. The hip area shown with point 2 is the interest of this work since most of the portable devices or sensors can be located around the hip practically. The hip acceleration determination experiments are carried out at three different speeds, which are walking, jogging and outrun. The subjects used a standard treadmill, on which the speeds are adjustable. The walking speed, the jogging speed and the outrun speeds are set to 3 km / h, 9 km / h and 15 km / h respectively. The waveforms including their amplitudes and frequencies are monitored and recorded. The data are published in APPENDIX A.

5.6 Anticipated EMF for human running

In order to predict the induced voltage as a result of human stride excitation of FR4 cantilever case study, the numerical model that already defines the physical system precisely is used. Since the average running frequency stated in the literature is about 2.75 Hz, a subject's running signal that has almost the same frequency is chosen from the experimentally obtained hip area accelerations in order to input this signal to the numerical model. Figure 5.9.a demonstrates this acceleration waveform obtained at 9 km / h running speed. Each peak corresponds to each stride. Note that for every two successive peaks, one of them is sharper than the previous one. The reason is the accelerometer placement point. The accelerometer is placed on the right side of the hip. Therefore, strides due to right foot are sharper than the left foot strides.

For the given input of figure 5.9.a, the simulations predict 39.5 μW rms power over R_L for the given subject's input. Figure 5.9.b shows the predicted emf signal. The numerical simulation is repeated with other 2 male subjects' signals for the same running speed. The stride frequencies and the resultant emf results are similar. In the experiment performed with square wave base excitation in section 5.2, the obtained rms power at 2.75 Hz input is

34 μW (see figure 5.5). The close power levels also prove that each stride is like an impulse to the scavenging system, which can be crudely approximated with a short pulse. The pulse excitation experiment in section 5.2 proves to be a good analysis method to mimic the acceleration data obtained using running human subjects.

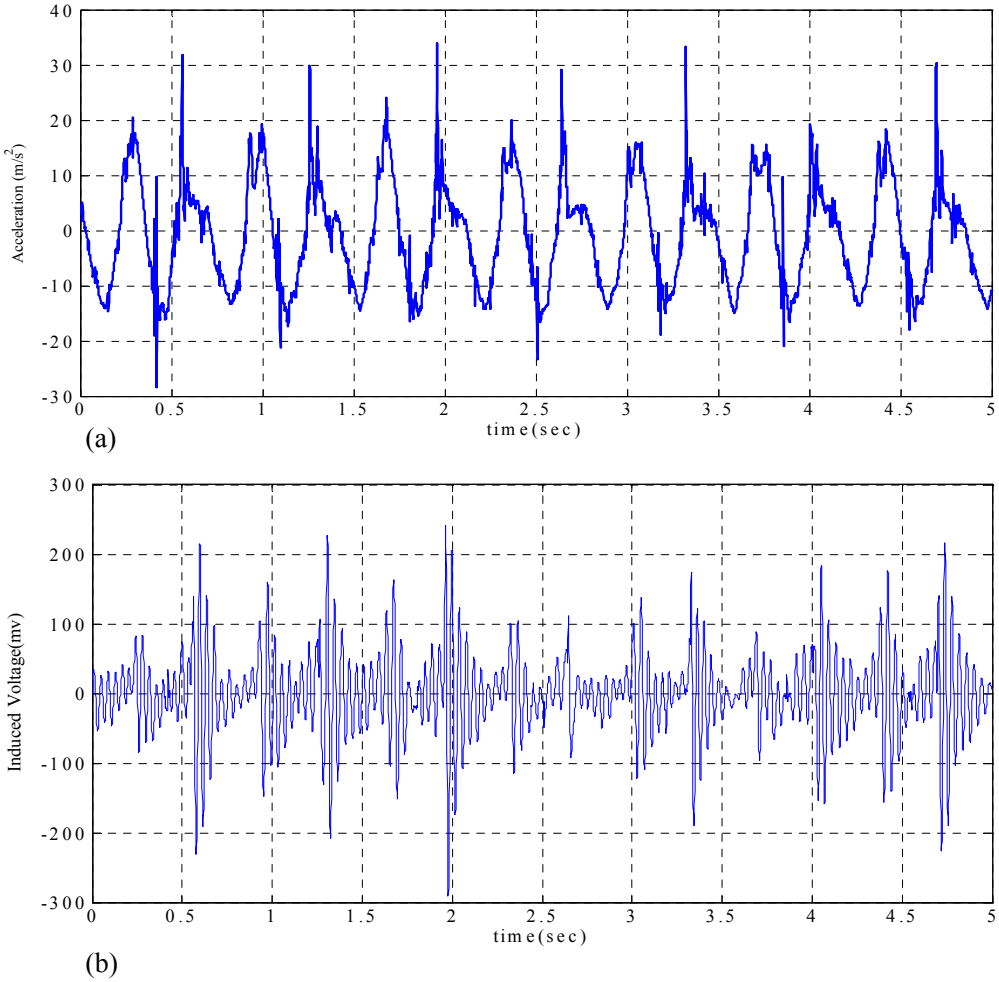

Figure 5.9. (a) Acceleration waveform obtained from a running test subject at hip area for jogging speed, (b) corresponding emf produced predicted by the simulation model.

5.7 Compact and broadband harvester

After the pulse drive experiments and numerical analysis with human hip acceleration waveforms, FR4 seems to be a promising material to design vibrating structures in order to design broadband devices. The FR4 cantilever design used during the experiments is chosen to test the performance and to validate the numerical model. Besides, it is easy to analytically express the resonant frequency of cantilever beams, which is given with the equation 4.3.

At this point, there is a need of designing a more advanced, compact and still low-frequency device in order to increase the power density. Keeping the harvester volume low is important since the wireless sensor nodes are also small volume devices as already discussed in Chapter 1. Moreover, placing a heavier magnet will cause much more oscillations as well as increased flux, so the magnet mass should be also increased.

Considering all these important design needs in order to increase power density, a unique actuator is first manufactured from very thin copper laminated FR4 sheets. The manufactured actuator is shown in figure 5.10 below.

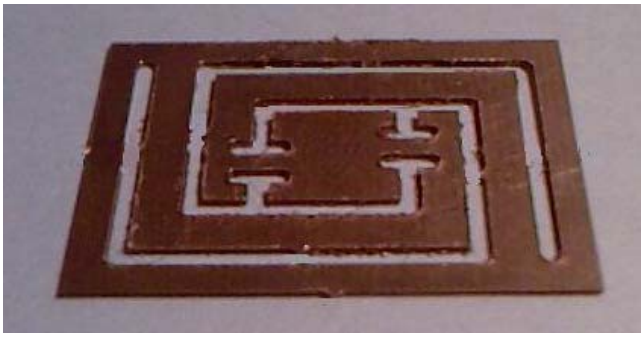

Figure 5.10 Fabricated FR4 structure with special spring design that gives compact form factor.

The design consists of 2 parallel cantilever beams connected to clear aperture with two other shorter cantilever springs. The total dimensions are 20 x 16 x 0.178 mm.

Using thin copper laminated FR4 aids to keep the spring constant low, thus the resonance frequency can be kept low. Another factor lowering the spring constant is the long crab-leg like cantilever beam geometry.

One may question how the placement of a heavier magnet on clear aperture is possible. The moving aperture has dimensions of 5 x 5 x 0.178 mm. The magnet used in FR4 cantilever design had a diameter of 15 mm and it is not possible to place a large magnet directly on this aperture. However, the magnet size limitation problem is solved using smaller spacer magnets as shown in figure 5.11.

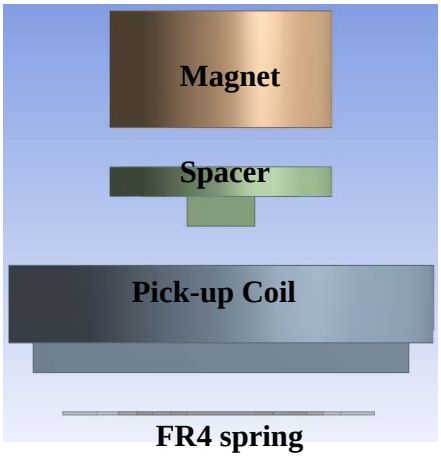

Figure 5.11 The components of the unique energy harvester design

A small rectangular FR4 spacer is first placed onto the aperture. On this piece, another larger FR4 piece that is circular is placed. By this way, a bigger magnet than the aperture that has a diameter of 13 mm and a height of 6 mm is placed onto the spacer. Thanks to spacer, the placed magnet (5.36 gr) is heavier when compared to the magnet used in FR4

cantilever design (around 4 gr), which results that environmental accelerations will be coupled to mass more, creating larger amounts of vibration. The springs then stays completely hidden under the spacer. The pick-up bobbin that has the same specifications with the one listed in table 1 embraces the spacer. Figure 5.12 demonstrates the components from isometric view.

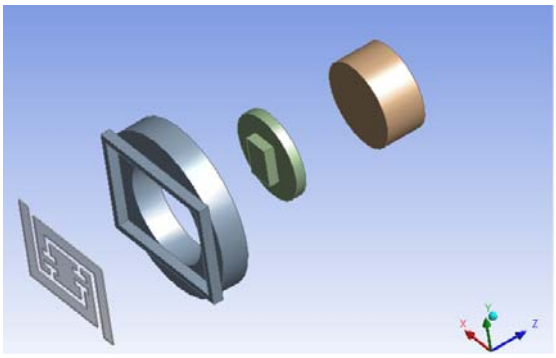

Figure 5.12 The spacer acts as a connector between the magnet and the FR4 spring.

Due to the actuator geometry, first two modes of the device are at low frequencies. These are torsion mode and out-of-plane mode, whose natural frequencies are 14.4 Hz and 24.4 Hz respectively. In the next section, effects of these two modes on energy generation will be investigated. The assembled FR4 EM harvester, abbreviated by calling the design *FR4-H*, is shown in figure 5.13 below.

Figure 5.13 Assembled energy harvester, FR4-H

5.8 Pulse drive experiments for FR4-H.

The same experiment performed in section 5.2 is repeated for FR4-H. Since the hip acceleration can be mimicked by a short pulse effectively, the square wave with the same amplitude and same duty is given to the EM energy harvester system via mechanical shaker. In addition, it is much easier to give pulse signals through the shaker. Since 1-5 Hz frequency region is the interest, figure 5.14 shows this region and the induced voltage values for open and closed loop operations.

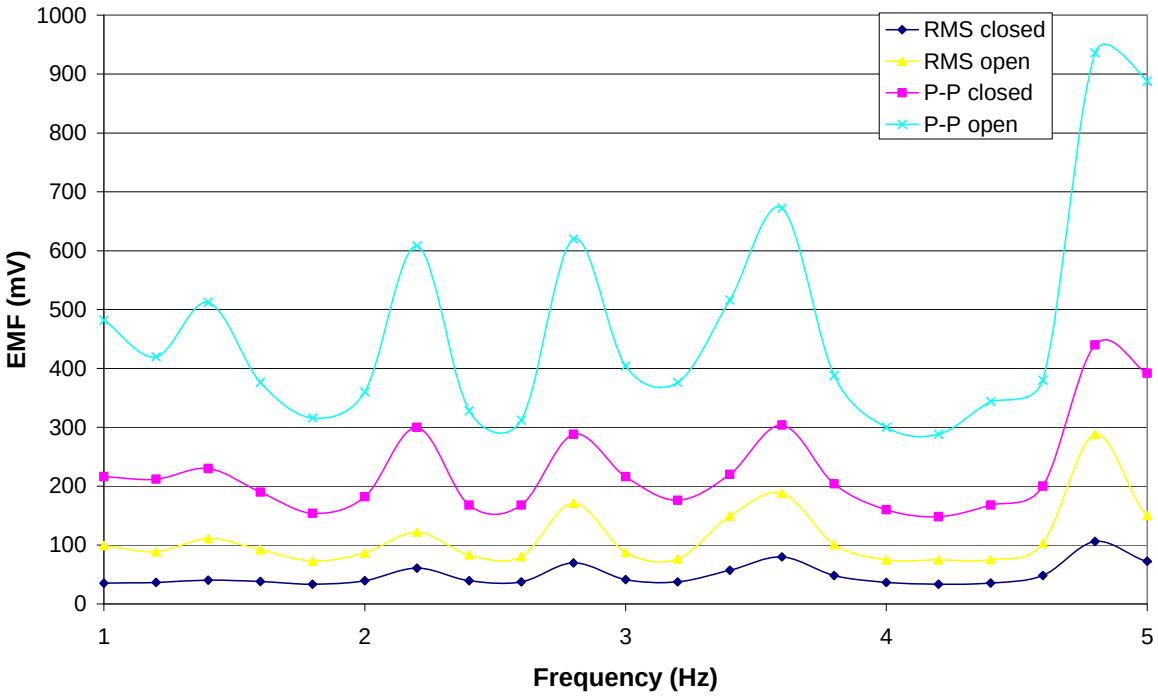

Figure 5.14 emf generation with FR4-H as a result of pulse drive.

It is observed that the compact design with spacers is more efficient than the cantilever based design. For comparison, the compact FR4-H design with spacer generates 49 μW

rms power over R_L at average running frequency that is 2.75 Hz, which is an improvement of 25% compared to the cantilever based design of Figure 4.5. In addition to emf improvement, the practical volume is reduced by 74% down to 4.1 cm^3 when compared to the FR4 cantilever design.

Since some asymmetries existing in the system, the torsion mode is also excited along with the out of plane mode.. This increases the number of local emf peaks for different frequencies, so the harvester becomes much more broadband. This is also remarkable feature of this design.

5.9 NPD for FR4-H

After the FR4-H design is tested for pulse drive, it is tested at resonance operation with sinusoidal input. In order to compare the device performance with the other energy harvesters in literature, resonance sinusoidal excitation is needed as explained in section 3.7. To emphasize again, nearly all reported energy harvesting devices are operated at their resonance frequency. The analytical reasons are well explained and reviewed in Chapter 3.

For calculations of NPD, the FR4-H energy scavenger is tested with a sinusoidal acceleration input of peak-to-peak amplitude $2m/s^2$ at the device resonant frequency of 24.4 Hz and compared with the reported scavengers in the literature [20]. An RMS power of 0.144 mW is obtained using a standard load resistance of R_L = 100 Ω.. The NPD is calculated with the equation3.45. Despite not being fully optimized, it demonstrates a notable normalized power density of 35.1 kgs / m^3. The comparison chart is demonstrated in figure 5.15.

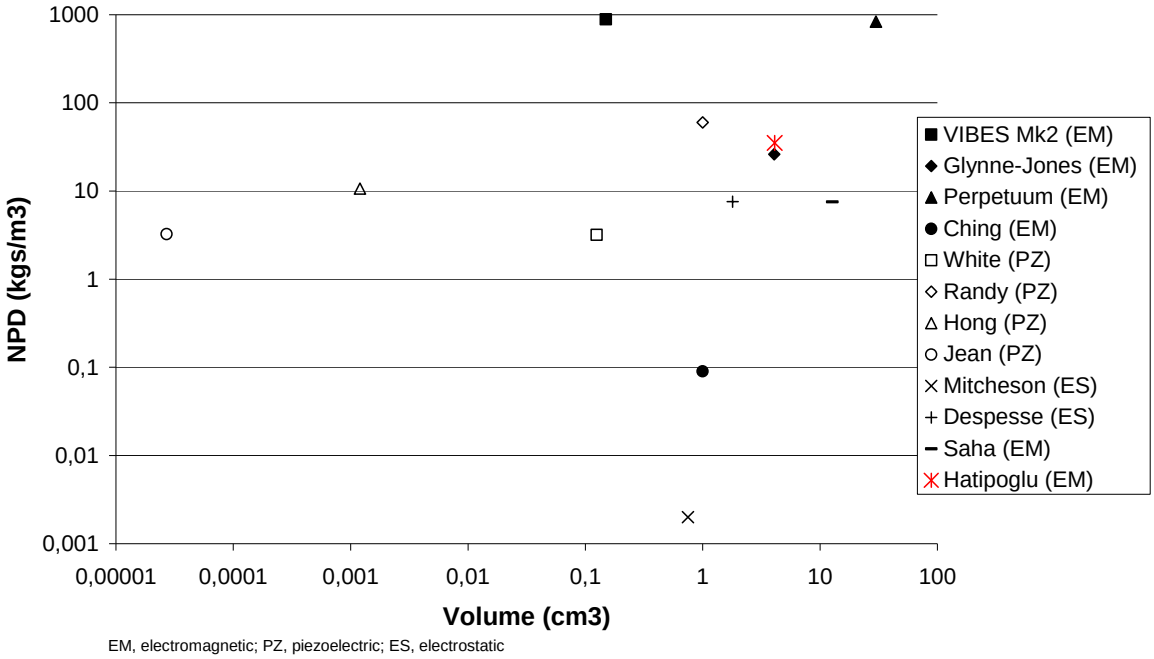

Figure 5.15 NPD comparison chart. FR4-H performance is notable.

Some of the better NPD values are obtained for higher resonant frequency (ω) devices and using vacuum conditions. NPD measured at resonant frequency is not a very good metric for practical applications involving environmental vibrations, but it is a good scale to compare the power outputs of various devices. Our design compares quite well with others in the literature. However, the real strength of our design is that it is not limited to narrowband sinusoidal excitations. It performs more favorably for low-frequency and broadband excitations, which is more important for practical applications.

5.10 Introduction to mechanical stoppers

Besides the spacer mechanism introduced in section 5.7 is used to place a bigger magnet in dimensions than the clear aperture, it also acts as a mechanical stopper. Due to spacer geometry, when the magnet tends to move in –z direction (see figure 5.12) and the springs deflect in –z direction, mushroom-like spacer contacts with the springs preventing them to deflect more than elastic limit.

In +z direction, the bobbin acts like a stopper too. It is placed on a FR4 platform, which has a known thickness. By manipulating this thickness, the spring deflection in +z direction is limited. The springs contact with the bobbin surface at a specific distance. In this design, the platform thickness is 1 mm.

In the following chapter, the mechanical stopper mechanism will be extended to tire applications while introducing non-linear spring and hard contact stoppers.

CHAPTER 6

TIRE ENERGY HARVESTER & NON-LINEAR MECHANICAL STOPPERS

6.1 Introduction

Energy harvesting for body-worn sensors and portable electronics from the human motion is reviewed in Chapter 5. However, the harvestable power from low frequency running of a human at the hip area is on the order of a few microwatts is not sufficient for most wireless sensor nodes since they generally consume power around 1 mW. Therefore, powering tire wireless sensors with our similar FR4 technology introduced in Chapter 4 and 5 is more attractive since there are broadband accelerations with rich harmonic content and high amplitudes in a rotating tire while the rotation frequency is typically less than 40 Hz. We believe FR4 based tire harvesters with their broadband response is a good solution for harvesting energy in such environments such as tire. It is important to power wireless sensors as long as a life of a tire. These tire sensors are important to monitor tire conditions.

In this chapter, the accelerations occurring due to tire-road contact is first introduced. The acceleration waveforms, amplitudes and modeling are reviewed. Then, the harmonic content of these waveforms are obtained. Later, compact FR4 based tire energy harvester design with mechanical stoppers is explained. Then, the tire energy harvester broadband response is tested with the mechanical shaker. Due to shaker limitation, high-g acceleration could not be given to the system. However, the power levels for high acceleration amplitudes are anticipated. Finally, a much more robust non-linear mechanical stopper

mechanism is introduced to the energy harvester. The contact analysis is performed in ANSYS in order to test the stopper performance. The chapter ends with discussion.

6.2 Tire-road contact acceleration

There is a need for broadband and robust scavenger for the wireless intelligent sensors, which are vitally used in tire applications like the Pirelli's Cyber™ Wheel [24] and SmarTire Systems [25] systems. The tire-road interaction, slip angle [26] and tire condition are tracked during the life of the tire via these wireless sensors. MEMS-based accelerometers or magnetostrictive sensors are placed into the inner liner of a tire. For Tire Pressure Monitoring Systems (TPMS), which are used to track the internal air pressure of the tire, the pressure sensors are placed onto the rim instead of the tire. These sensors should be powered via an energy source. Power harvesting for these sensors through contact accelerations seems a very good solution.

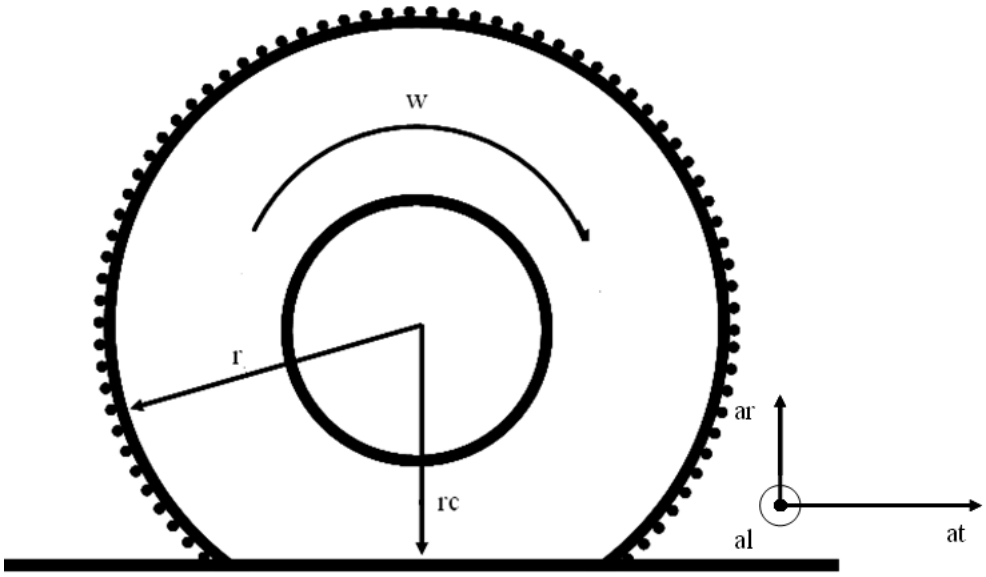

Figure 6.11 A typical tire. The contact deformation region is exaggerated. The three contact acceleration directions are shown.

During tire rotation, some portion (about 10-15% of the perimeter) of the tire contacts with the road as shown in Figure 6.3. This contact region of a tire elastically deforms and becomes almost flat due to weight of a vehicle. This deformation and then un-deformation occurs periodically. During this cyclic deformation, accelerations occur due to this contact in three different directions, which are lateral (a_l), tangential l(a_t) and radial (a_r).

These accelerations are perfect source to power the sensors. Figure 6.4 demonstrates an example of the expected tangential acceleration waveform occurring during the contact for a vehicle having a translational speed of 30 kph, resulting in 4.65 Hz periodic excitation considering the tire scavenging system is placed along the inner liner of a 195/50 R15 tire.

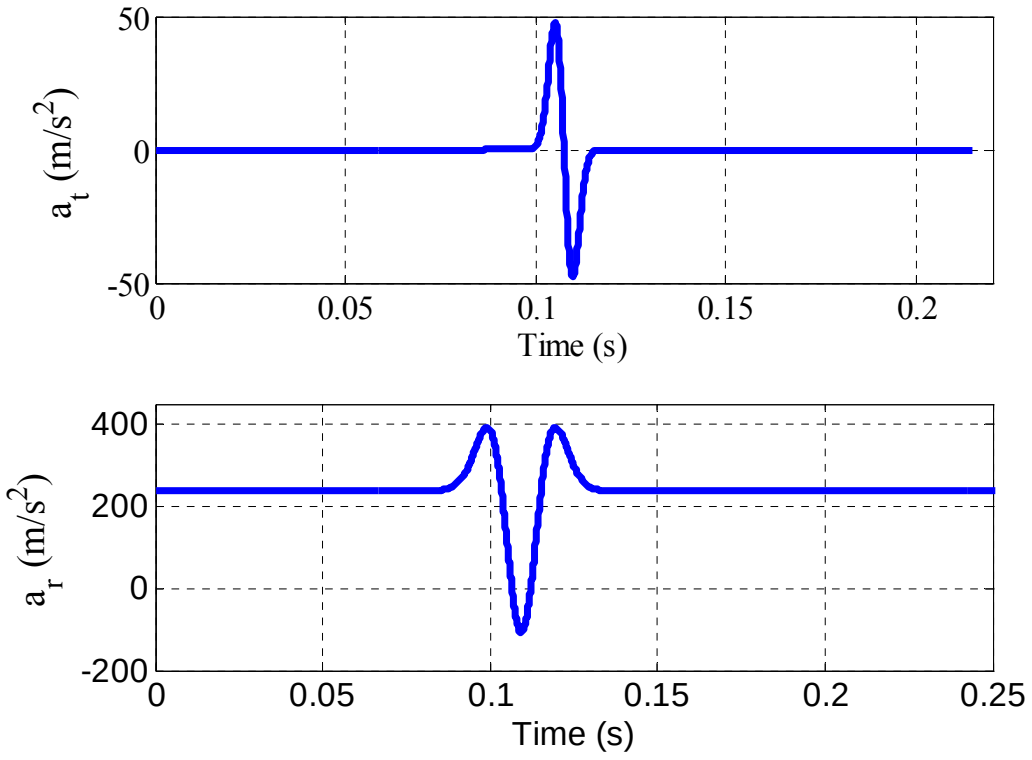

Figure 6.12 Typical tangential and radial acceleration waveforms for 30 kph vehicle speed [27].

The tire-road contact supplies tangential acceleration amplitudes reaching up to 300g and radial acceleration amplitudes reaching up to 1500g depending on the tire operating conditions [27]. The acceleration amplitudes are proportional to translational speed square. Besides, the magnitude and the shape of the tangential waveform fit well with the first derivative of Gaussian pulse whereas the radial acceleration waveforms can be expressed with the second derivative of a Gaussian function. As an example, tangential acceleration waveform shown in Figure 6.4 can be expressed with the derivative of a Gaussian equation;

$$\ddot{y}(t) = 0.18e^{(-(T/2-t)^2/2\sigma^2)} \tag{6.1}$$

where T is the period (0.215 sec for 30 kph) and σ is the variable determining the duty cycle (0.0023 for 30 kph). The contact duty-cycle is estimated as 10-15 % as indicated before.

The tire harvester is planned to be mounted onto the inner liner of a tire such that the tangential acceleration will cause out-of-plane deflection of the moving magnet and the radial and lateral accelerations will cause torsional deflection. However, tangential accelerations are selected as the main vibration source since the radial and lateral accelerations have also a DC component. Therefore, the radial and lateral accelerations are not tested in the shaker experiments, but the tangential acceleration waveforms are used instead. On the other hand, a stopper mechanism is inserted into the system to avoid high torsional deflections due to radial and lateral accelerations. This is explained more detailed in the following sections.

Owing to these high acceleration amplitudes, it is also impossible to design a resonant device with high efficiency due to inevitable mechanical failure. Therefore, the target is to harvest power off-resonance as it is done in Chapter 5. In order to design the tire energy harvester at optimum levels, the frequency spectra for different wheel translational speeds are thus obtained. Figure 6.5 demonstrates the frequency spectra of the tangential accelerations occurring as a result of tire-road contact. The short-pulse like waveforms

have rich harmonic content increasing the power harvesting efficiency of our system at off-resonance operation. Furthermore, the harmonics frequency range is broad.

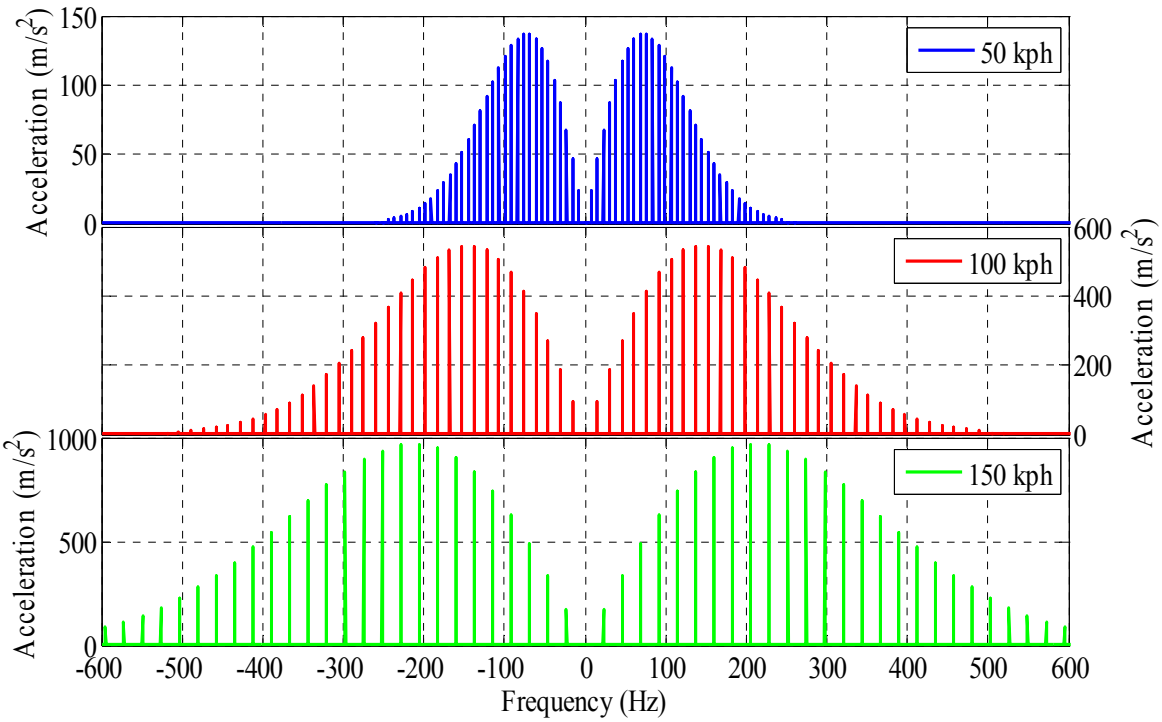

Figure 6.13 The Frequency Spectra of expected tangential accelerations occurring at selected translational vehicle speeds.

6.3 Tire Energy Harvester

According to harmonic distribution and the energies of these harmonics, the tire energy harvester resonance frequency is set to 46 Hz. This frequency is selected since the tire harvester is expected to generate emf for a wide range of vehicle speeds. **Figure 6.6** shows the frequency spectra of different speeds plotted over each other. At 46 Hz frequency, the harmonics related to different speeds coincide and they have notable energy.

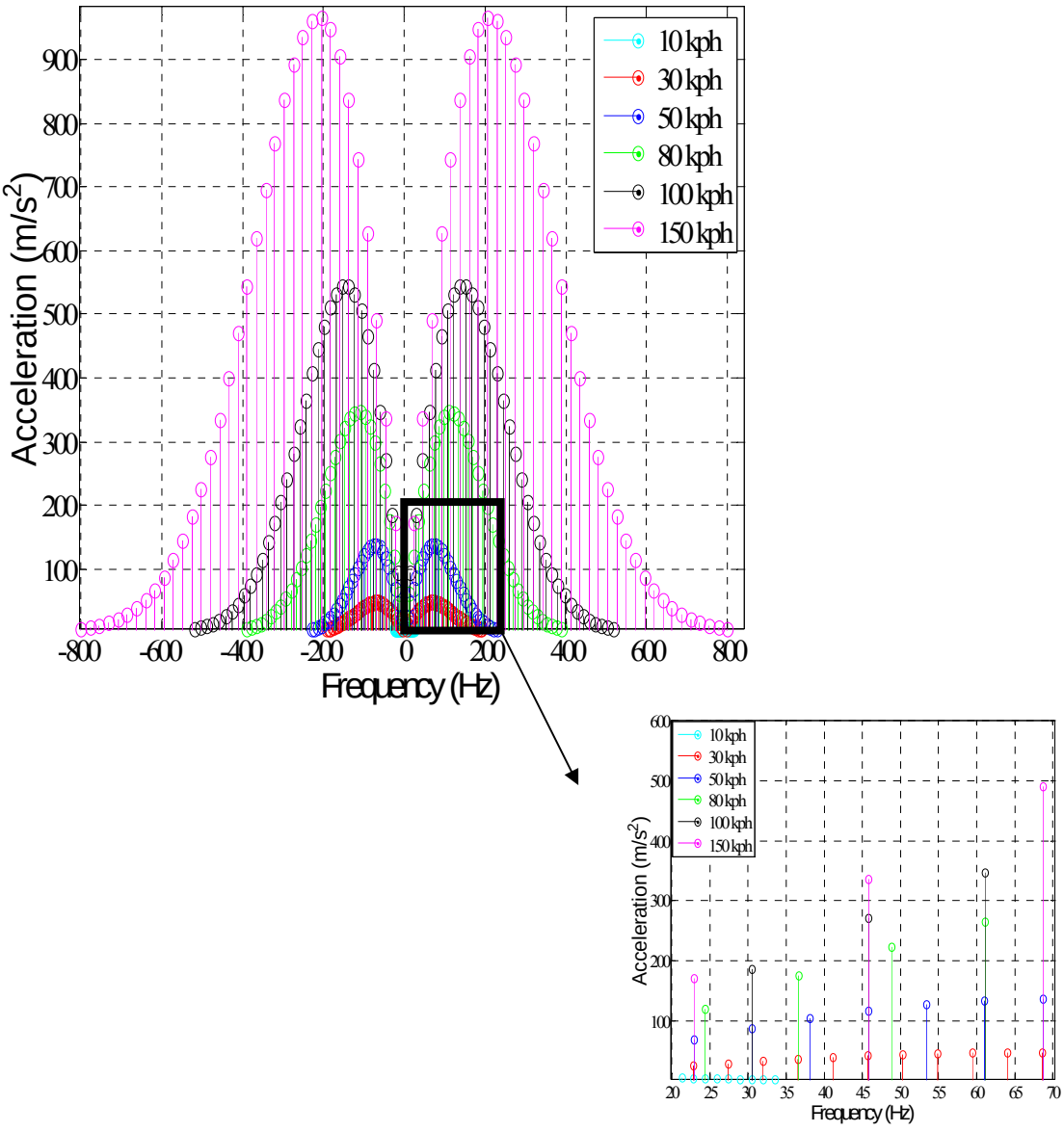

Figure 6.14 Frequency spectra of targeted vehicle speed range that is between 10 kph to 150 kph. At 46 Hz (zoomed box), the harmonics for different speeds coincide. Therefore, it is reasonable to design the harvester resonance frequency at 46 Hz.

The tire energy harvester shown in **Figure 6.7** has a similar design with the compact FR4 harvester designed for human running motion (see Chapter 5). Again, the movable FR4 spring is hidden just in the bobbin, which has the same specifications given in table 4.1.

Figure 6.15 Tire Energy Harvester

Since tire experiences high amplitude accelerations during the rotation, the spacer mechanism explained in section 4 is incorporated into the system to act as a mechanical stopper. However, four smaller Nd stacked magnets beneath one oversized Nd magnet (Br ≈ 1 Tesla) on the top are utilized as spacers rather than using FR4 as a spacer. The dimensions of the stacked magnets and the oversized magnets are given in table 6.1.

Table 6.1 Oversized and spacer magnet dimensions

Magnet	radius (mm)	height (mm)
Oversized	10	2
Spacer 1	7.5	2
Spacer 2	4	3
Spacer 3	2.5	1.5
Spacer 4	2.5	1

The schematic of stacked magnet and FR4 platforms assembly is shown explicitly in figure 6.6. The smaller magnets completely stay inside the pick-up coil enabling to achieve a more compact design.

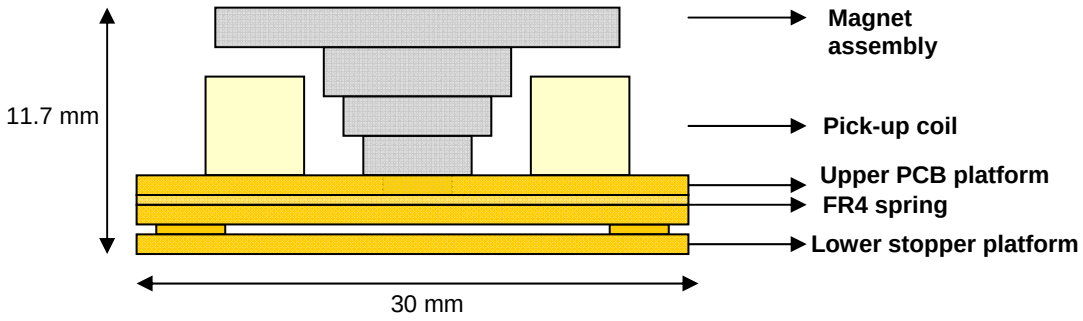

Figure 6.6. The FR4 spring, having a very similar design with the spring shown in figure5.9, is sandwiched between two thicker FR4 platforms. This time, the oversized magnet, lower stopper platform and bobbin act as mechanical stoppers.

Compared to single magnet configuration discussed in Chapter 5, the novel stacked magnet configuration supplies a better magnetic flux density gradient, which in turn generates higher levels of emf. Figure 6.7 demonstrates the magnetic flux density over magnet radii as a function of z. When this flux distribution is compared with the one in figure 4.8, one can easily realize that the magnetic flux density gradient is higher and broader. The maximum flux density value is also higher for the stacked magnet configuration when compared to the single magnet configuration.

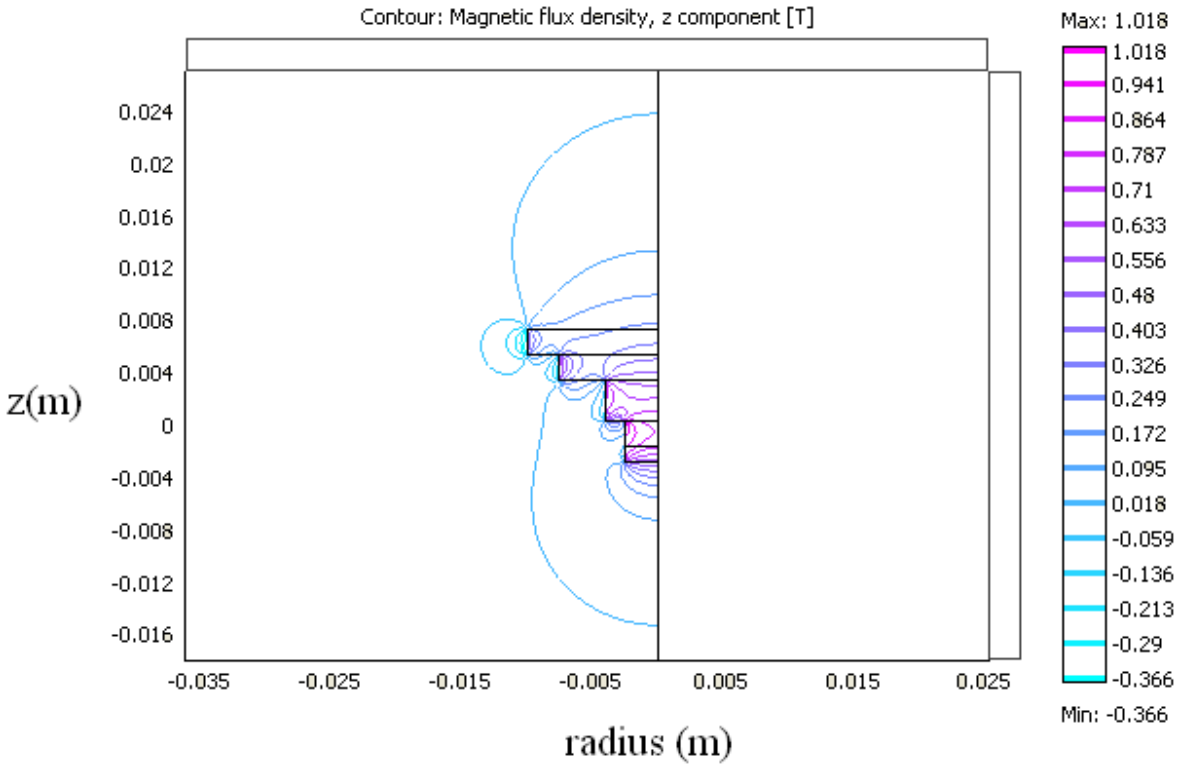

Figure 6.7 Contour plot of magnetic flux density, z component. The unit is Tesla. Note that the contour lines are wider and the maximum and minimum flux values are broader.

The main novelty of the design is being compact as well as efficient. The efficiency is increased by utilizing *Nd* magnets as spacers while supplying a better flux density gradient. In order to test the performance of the tire energy harvester, shaker experiments are carried out as tangential contact accelerations are used as input to the system.

6.4 Shaker experiments

In order to test tire scavenger performance, shaker experiments are performed for various vehicle speeds. The expected tire-road contact tangential acceleration waveforms similar to shown in figure 6.2 are given by the shaker over an arbitrary signal generator.

Since the shaker is driven with displacement data, the integral of the Gaussian function, which is the error function, is fed to the shaker to obtain the desired shaped acceleration waveforms. Figure 6.8 exhibits the tire energy harvester's wideband response to acceleration inputs for different speeds (contact frequencies). The acceleration input is fixed at constant amplitude that is 1.5g. In actual operation, the amplitudes are increasing as the vehicle speed increases. However, the high acceleration values could not be achieved by the shaker at low frequencies due to shaker frequency-amplitude limitations. Nevertheless, the FR4 tire harvester response is observed.

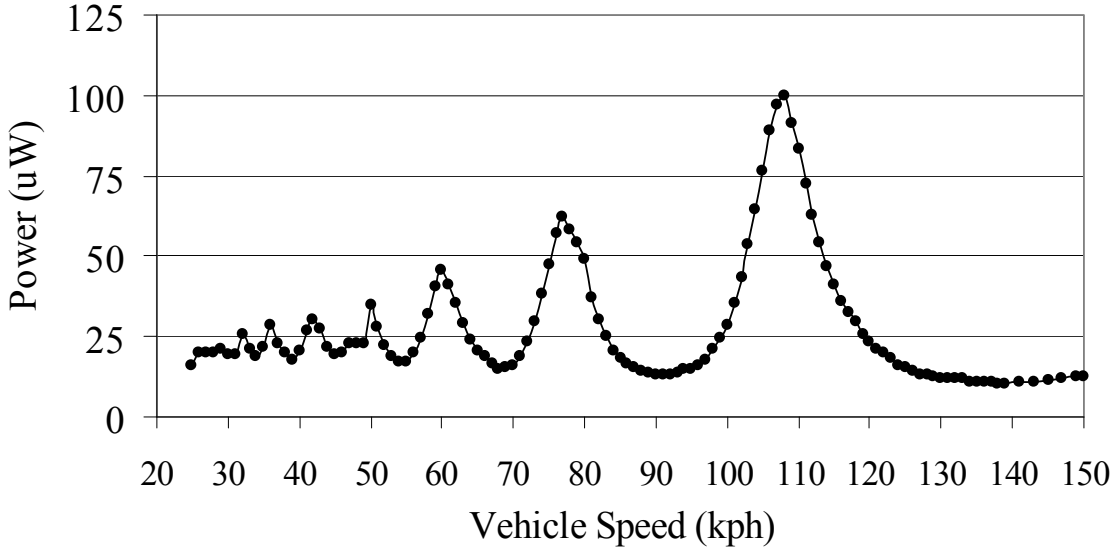

Figure 6.8. Power across R_L versus various vehicle speeds for 3g p-p tangential acceleration input. Corresponding contact frequencies can be calculated using the conversion factor 1 Hz = 6.57 kph.

As the harmonics of the energy harvester match with the excitation frequency, local peaks in the power are observed. Since the mechanical *Q* factor of the structure is low unlike silicon based energy harvesters, the power output is broadband. Notice that each

peak is fairly wide. Therefore, electrical induction is not limited just to resonance operation. Indeed, it is extended to off-resonance operation over a wide range of frequencies. This is a remarkable result and an important advantage of FR4 based harvesters over MEMS based harvesters.

In order to estimate the power output in actual operation, a final shaker experiment is carried out. For five different vehicle speeds, tangential acceleration amplitude is increased to the limits of the shaker for each frequency. Since the shaker can give higher amplitudes at higher frequencies, the acceleration amplitudes are increased during testing tire energy harvester. As shown in figure 6.9, the tire energy harvester can generate 0.4 mW power across R_L at off-resonance operation for 15 g p-to-p tangential acceleration input corresponding to 150 kph speed.

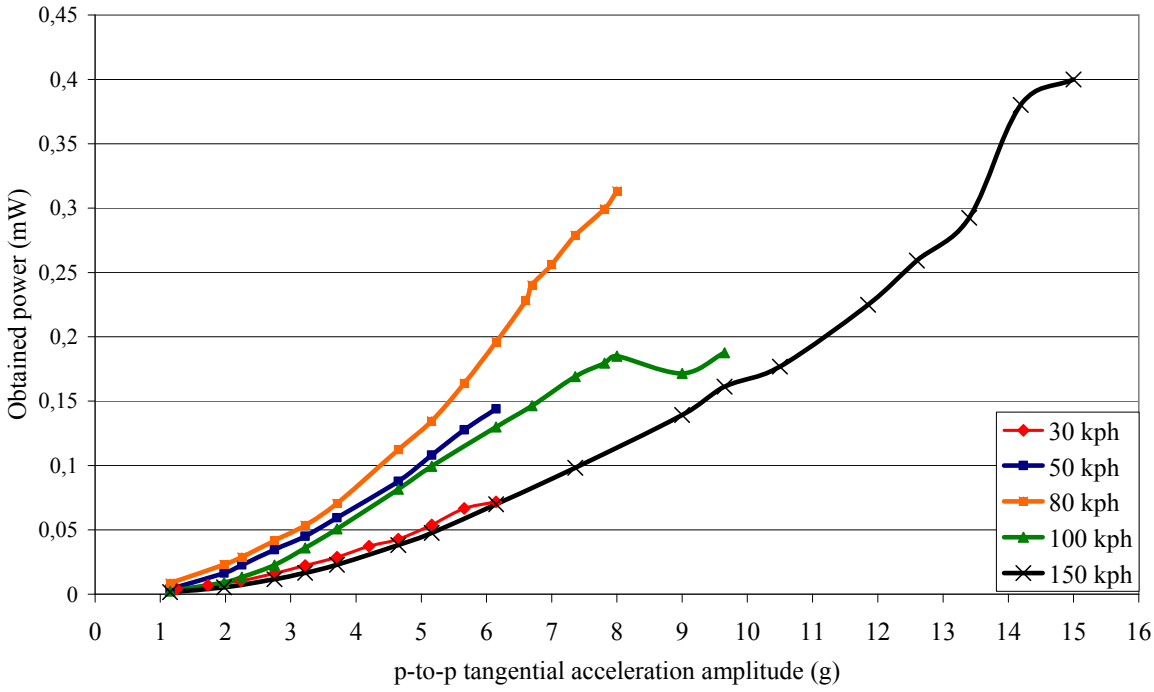

Figure 6.9 Power across R_L = 100 Ω versus increasing acceleration amplitude for 5 different vehicle speeds.

The acceleration inputs tested using the shaker is limited to less than $1/10^{th}$ of the accelerations in actual operation. Considering the fact that 150 kph vehicle speed is a local minimum at power generation (Figure 6.9), the power levels at coinciding harmonics for a single device could easily go beyond 1 mW range, which is sufficient to power wireless tire sensors. Multiple FR4 scavengers can be connected in series to increase the power further.

6.5 Effects of hard mechanical contacts

In section 6.4, the testing amplitude was chosen as mechanical contact does not occur. In order to observe the effects of the mechanical contacts formed by the bobbin and stopper platform, the tangential acceleration input is increased to 8g peak-to peak amplitude. The emf generated with tire energy harvester involving contact versus non-contact cases are shown in figure 6.10.

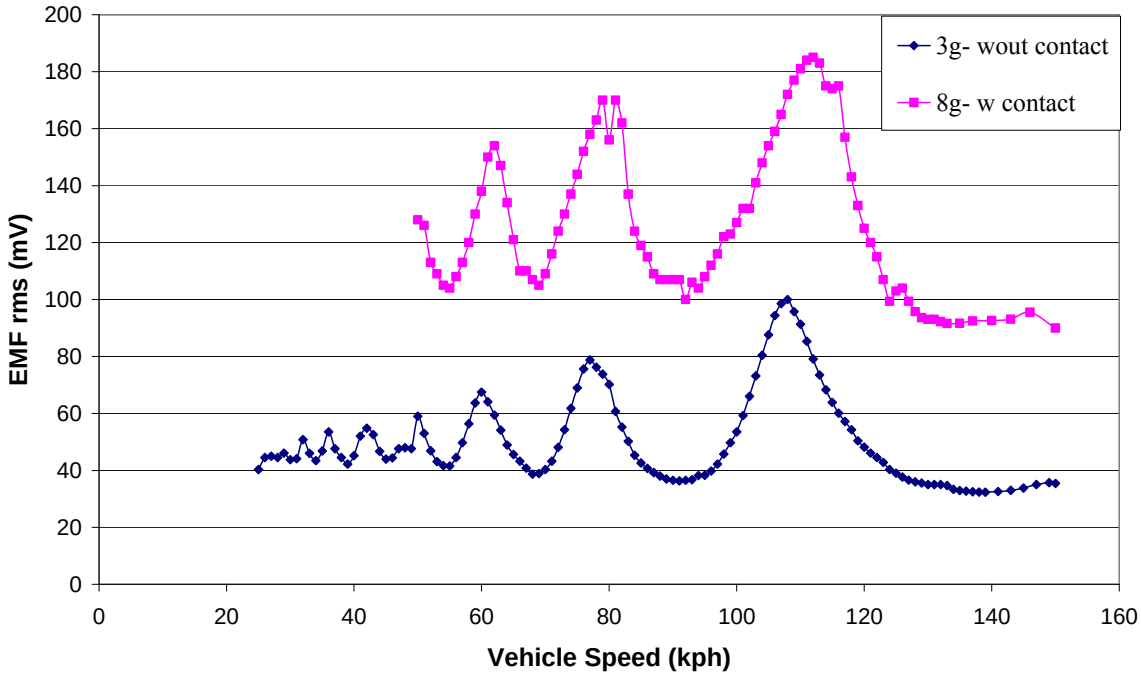

Figure 6.10 emf generated as a result of tangential accelerations with and without contact

The peaks at harmonics are distorted at contact case and the resonance frequency shifts a few Hertz due to increased stiffness at contacts. While the stoppers limit the deflection of the FR4 spring, some of the energy is lost due to contact as expected. Nevertheless, emf generation is still notable. The effect of contacts can be also observed from the shape of the emf waveforms. Figure 6.11 shows the two cases of emf generation; at contact case versus at the non-contact case for constant amplitude sinusoidal excitation. The frequency and amplitude is chosen arbitrarily.

(a)

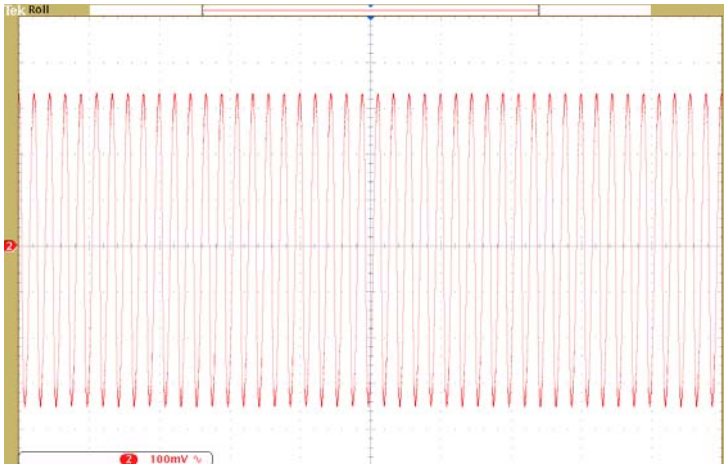

(b)

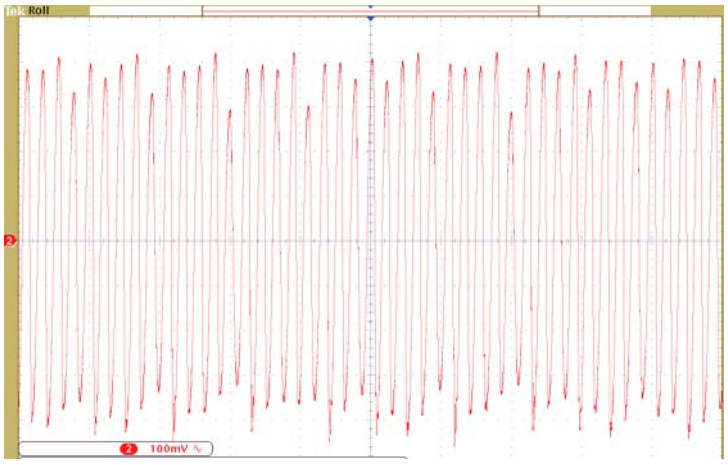

Figure 6.11 a) emf generation at non-contact case b) emf generation at contact case.

6.6 Break test at resonance

Despite the fact that tire energy harvester targets emf production at off-resonance, it is also tested at its mechanical resonance frequency with sinusoidal acceleration input in order to test how robust is the stoppers and the FR4 spring. Figure 6.12 shows the break test at resonance. The emf is recorded for NPD calculation purposes.

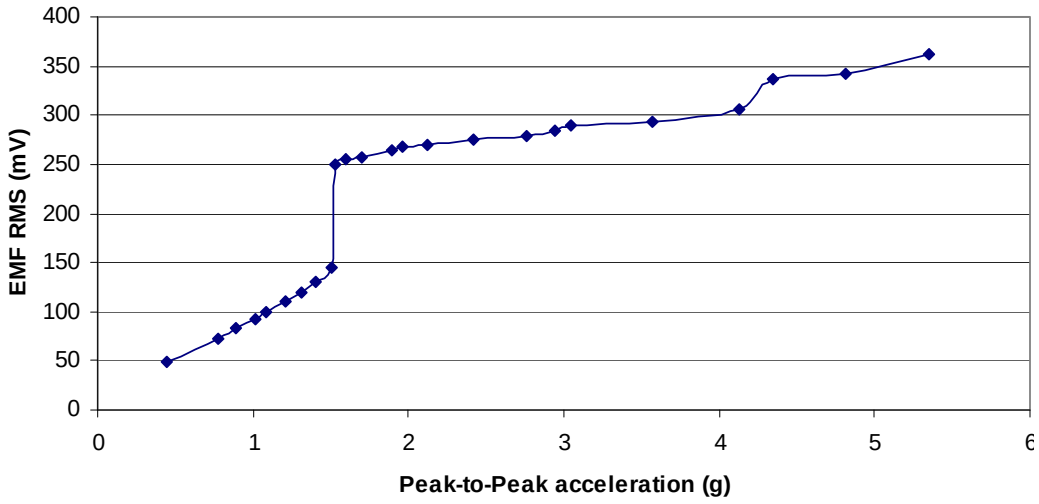

Figure 6.12 Break test at resonance for sinusoidal input.

Resonance operation is the extreme case as indicated. However, the device failed for 5.5g p-to-p acceleration input. The failure occurred due to shear at the clear aperture connection regions to spring arms as shown in figure 6.13. Even though the contact acceleration frequencies never reach to mechanical resonance frequency of the tire harvester, the springs should be robust for any case of excitation frequency.

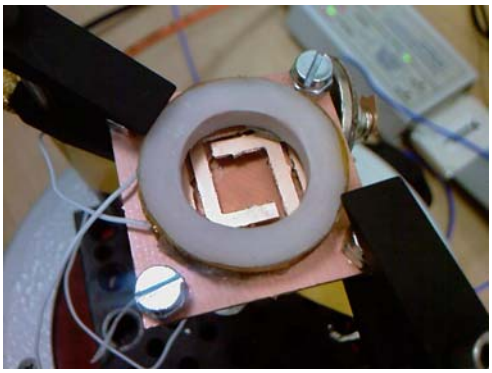

Figure 6.13 The failed specimen

6.7 Non-linear mechanical stoppers

The stopper mechanism is needed since tire experience high-g contact accelerations. In order to withstand to these accelerations, mechanical stoppers prove themselves to be a good mechanism. The hard contact mechanism effects and functionality are observed experimentally in the previous section.

In order to improve the stopper mechanism, non-linear mechanical stoppers are introduced in this section. These newly proposed stoppers are much more robust mechanism and efficient compared to hard contacts.

The tire energy harvester design introduced in section 6.6 is modified with the non-linear mechanical stoppers. The stacked magnet configuration is placed on top of the FR4 spring actuator, which is sandwiched between upper and lower FR4 platforms. Above and below of the magnet configuration, two FR4 stoppers whose spring constants are comparable with the actuator is placed. If the magnet deflects due to tangential accelerations, the stoppers deform due to magnet contact. Once the magnet and the stopper are in contact, the spring constant is increased, so the magnet deflection is decreased. If more stoppers are introduced within the deformation region of the magnet, the stoppers

behave as non-linear springs. In other words, the spring constant increases as the deflection of the magnet increases. By this way, the magnet deflection is limited. Compared to hard mechanical contacts, less energy is lost during contacts. Furthermore, the stopper springs store some of the energy and give this to the magnet after the contact separation.

The contact springs can be cascaded with specific distances. However, two stoppers are adequate for tire energy harvester. Figure 6.14 shows the non-linear stopper mechanism.

a)

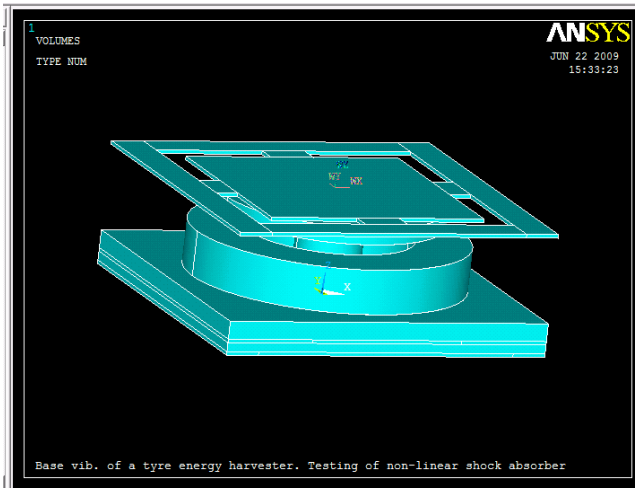

b)

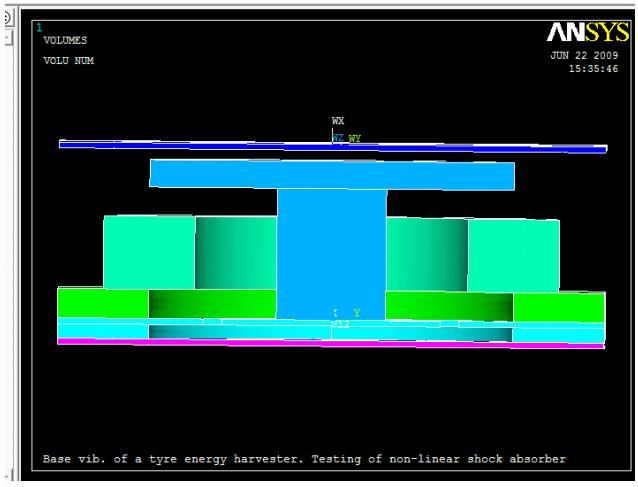

Figure 6.14 a) The tire harvester with non-linear stopper mechanism. b) The cross sectional view of the system.

6.8 Contact Analysis

Due to the limitations of the mechanical shaker in our facilities, the high-g accelerations are simulated in FEM package, ANSYS. In the simulation environment, the tire-road contact accelerations including tangential and radial waveforms are simulated using transient analysis with contact. The acceleration amplitudes can reach up to 300 g in tangential direction and 1500 g in radial direction [27]. The FR4 stopper springs are designed as to survive under these inputs. As it is discussed in previous sections, the radial accelerations cause torsional vibration whereas the tangential accelerations cause out-of-plane vibrations. For both types of inputs, the introduced system shown in figure 6.14 is able to deflect in the limits of elastic deformation. The FR4 spring can deflect ±0.8 mm without any plastic deformation. The stopper springs, being stiffer than the FR4 spring, are placed 0.4 mm away from the magnet configuration at rest position. Therefore, the contact occurs at 0.4 mm above and below the magnets as shown in Figure 6.15.

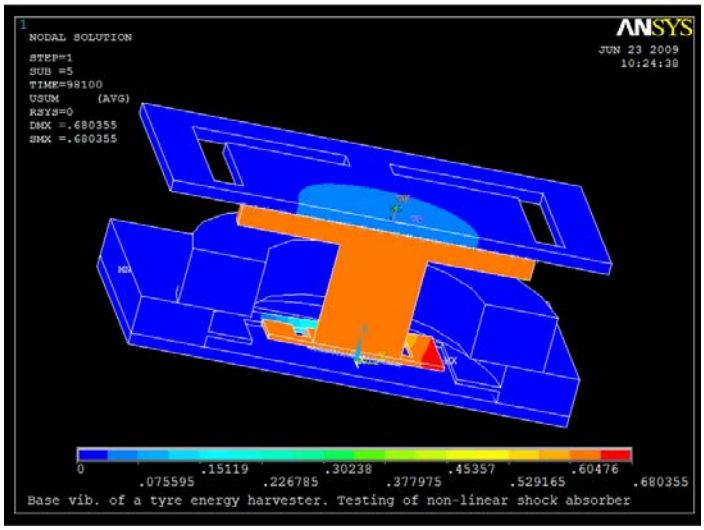

Figure 6.15 The FR4 spring and FR4 stopper spring contact condition at one of the extremum points for 300g acceleration amplitude. The contact occurs at 0.4 mm deflection. Symmetry boundary condition is used in order to reduce the simulation cost.

After contact, the spring constant is increased to the sum of the FR4 spring and FR4 stopper. Thus, the deflections are decreased at contacts as the system has a non-linear spring constant.

CONCLUSIONS

In this work, copper laminated FR4, which is a well known PCB material is proposed as an alternative material to design low frequency and broadband EM energy harvesters that are used to power wireless sensor nodes via environmental vibrations. Generally, the devices in literature are MEMS based and have frequencies on the order of kHz while being narrowband due to low intrinsic damping. However, environmental vibrations are broadband and generally between 0-100 Hz. FR4 with its high intrinsic damping and lower stiffness value compared to silicon enables to design low frequency harvesters.

Before testing the FR4 performance, the governing equations and modeling of an EM energy harvesting system is given. The basic laws like Faraday's law of induction and Lenz law are clearly explained. The EM energy harvesting system can be modeled as a reduced second order mass spring damper system with base excitation. The induced power over a load resistance for sinusoidal and non-sinusoidal periodic excitation signals are driven.

These equations are later used to develop a numerical magneto-electro-mechanical model. This model offers a good numerical testing environment, which was lacking in the literatuıre. Once the numerical model including the magnetic damping effects is established, FR4 performace is first tested with preliminary design that is a simple cantilever. FR4 cantilevers with different natural frequencies are manufactured from thin sheets of FR4. One of them is studied as a case study to validate the numerical model and observe the performance. The cantilever system is tested with pulse excitation via mechanical shaker. This kind of excitation is chosen to mimic the strides of a human. Considering every stride as an impulse, the FR4 cantilever system is driven with pulse with closer duty cycle of human running. Despite the variants in magnetic and mechanical domain, the numerical model fitted well with the experiments.

Then, the real human running data at the hip area are collected experimentally with accelerometers. These signals are given to numerical model to find out the generated emf as human runs. The results indicate that about 40 μW power over a load resistance of 100 Ω with 15 m/s^2 acceleration input is obtained.

A more compact and robust harvester system is later developed with built-in mechanical structures. The system has notable NPD values. The shaker experiments with pulse excitation is repeated for this system and power generation improved 25% while reducing the volume by 74% when compared to the FR4 cantilever beam case.

This compact design lead the author to design a more efficient device with stacked magnet configuration, which increases the magnetic flux gradient. This particular design explained in Chapter 6 is targeted to be used inside a rotating tire. Due to contact of the tire with road, contact accelerations occur. These accelerations are given to the system with arbitrary signal generator through the mechanical shaker. Over the same load resistance, 0.4 mW power is obtained at 150 kph vehicle speed for 15g p-p acceleration. Due to shaker limitations, high-g accelerations that are expected in actual operation could not be supplied. However, an anticipated power trend is obtained and the power levels are expected at mW regions which is sufficient to power tire wireless sensors.

Finally, a more robust non-linear stopper mechanism is offered. This mechanism works as spring stiffening when the magnet deflection tries to pass over the desired levels. In other words, the deflection of the magnet is limited within the elastic region by stiffening the actuator spring. This system is modeled in FEM package and simulated with high-g accelerations. However, the system is not tested experimentally yet.

The future work includes the testing of these non-linear stoppers and the mounting of the system inside a real tire. Then, the performance of tire energy harvester may be observed under actual operation. In any case, FR4 proves itself to be a good material for energy harvesting applications though.

BIBLIOGRAPHY

[1] Henry A. Sodano, Daniel J. Inman and Gyuhae Park "A Review of Power Harvesting from Vibration Using Piezoelectric Materials" T*he Shock and Vibration Digest* 2004; 36; 197

[2] Joseph A. Paradiso, Thad Starner, "Energy Scavenging for Mobile and Wireless Electronics," IEEE Pervasive Computing, vol. 4, no. 1, pp. 18-27, Jan.-Mar. 2005, doi:10.1109/MPRV.2005.9

[3] http://wireless.industrial-networking.com/images/art_images/19wsnarticle2.gif

[4] http://webs.cs.berkeley.edu/800demo/dots.jpg

[5] Urey H, Holmstrom S and Yalcinkaya A D 2009 Electromagnetically Actuated FR4 Scanners IEEE Phot. Tech. Let. 20 30-32

[6] Isikman S O, Sprague R B and Urey H 2009 FR4 laser scanner with dynamic focus IEEE Phot. Tech. Lett. 21 233-235

[7] Urey H, Holmstrom S and Yalcinkaya A D 2008 Electromagnetically actuated FR4 Scanners IEEE Phot. Tech. Lett. 20 30-32

[8] A.H. Epstein, S.D. Senturia, G. Anathasuresh, A. Ayon, K. Breuer, K-S Chen, F.E. Ehrich, G. Gauba R. Ghodssi, C. Groshenry `Power MEMS and Microengines` Rm. 3 1-265, Massachusetts Institute of Technology

[9] Amirtharajah R and Chandrakasan A P 1998 Self-powered signal processing using vibration-based power generation IEEE J. Solid-State Circuits 33 687–95

[10] Neil N. H. Ching, Gordon M. H. Chan and Wen J. Li Hiu Yung Wong and Philip H. W. Leong ``PCB INTEGRATED MICRO-GENERATOR FOR WIRELESS SYSTEMS`` Proceedings of the international symposium on Smart Structures and Microsystems, August 2000

[11] El-Hami M, Glynne-Jones P, James E, Beeby S P, White N M, Brown A D, Ross J N and Hill M 2001 Design and fabrication of a new vibration-based electromechanical power generator Sensors Actuators A 92 335–42

[12] Neil N. H. Ching1, H. Y. Wong2, Wen J. Li1,*, Philip H. W. Leong2, and Zhiyu Wen3 ``A Laser-micromachined Multi-Modal Resonating Power Transducer for Wireless Sensing Systems`` Sensors and Actuators A: Physical, November 2001.

[13] Kulah H and Najafi K 2004 An electromagnetic micro power generator for low-frequency environmental vibrations Micro Electro Mechanical Systems—17th IEEE Conf. On MEMS (Maastricht), 237–40

[14] Das S., Arnold D. P., Zana I., Park J. -W., Lang J. H. and Allen M. G., "Multi-Watt electric power from a microfabricated permanent-magnet generator", The MTL Annual Research Conference ,MARC 2005, Waterville Valley, NH, January 26-27, 2005, pp. 287-290.

[15] Buren T, Troster G 2007 Design and optimization of a linear vibration-driven electromagnetic micro-power generator, Sensors and Actuators A: Physical 135 765–775

[16] Mitcheson P D, Green T C, Yeatman E M and Holmes A S 2004 Architectures for vibration-driven micropower generators *IEEE J. Microelectomech. Syst* **13** 429–40

[17] Beeby, S. P., Tudor, M. J. and White, N. M. (2006) Energy harvesting vibration sources for microsystems applications. *Measurement Science and Technology*, 17 (12). R175-R195.

[18] Architectures for vibration-driven micropower generators, Mitcheson, P.D.; Green, T.C.; Yeatman, E.M.;Holmes,A.S. *Microelectromechanical Systems, Journal of* On page(s): 429- 440, Volume: 13, Issue: 3, June 2004

[19] Singiresu S. Rao, Mechanical Vibrations (3rd edition), Addison-Wesley Publishing Company,1995

[20] Beeby S P, Torah R N, Tudor M J, Glynne-Jones P, O'Donnell T, Saha C R and Roy S 2007 A micro electromagnetic generator for vibration energy harvesting *J. Micromech. Microeng*., **7** 1257–1265

[21] A dissertation submitted to the SWISS FEDERAL INSTITUTE OF TECHNOLOGY ZURICH for the degree of Doctor of Sciences presented by Thomas von Buren "Body-Worn Inertial Electromagnetic Micro-Generators"

[22] Buren T, Troster G 2007 Design and optimization of a linear vibration-driven electromagnetic micro-power generator, Sensors and Actuators A: Physical 135 765–775

[23] Young, W.C.; Budynas, R.G. (2002). Roark's Formulas for Stress and Strain (7th Edition).. McGraw-Hill. Online version available at: http://knovel.com/web/portal/browse/display?_EXT_KNOVEL_DISPLAY_bookid=475&VerticalID=0

[24] Zhang T, Jiang C, Xu H and Mao J 2007 Permanent-magnet longitudinal fields for magnetostrictive devices *J. Appl. Phys.* **101**

[25] J.B. Morin_, P. Samozino, K. Zameziati, A. Belli. "Effects of altered stride frequency and contact time on leg-spring behavior in human running" Journal of Biomechanics 40 (2007) 3341–3348

[26] Pirelli Tire: United States. Pirelli- Cyber™ Wheel. US: Pirelli & C. S.p.A. ; [Updated 2006 July 14; cited 2009 June 14]. Available from: http://www.us.pirelli.com/web/technology/technology-revolution/cyber-wheel/default.page

[27] Bendix CVS Canada Inc. SmarTire Systems. Richmond, BC, Canada: Bendix Commercial Vehicle Systems LLC. [Cited 2009 June 14]. Available from: http://www.smartire.com/

[28] Guillaume Baffet, Ali Charara and Daniel Lechner. Estimation of Tire-Road Forces and Vehicle Sideslip Angle. Advances in Robotics, Automation and Control PP-138

[29] APOLLO Intelligent tyre for accident-free traffic, Technical Research Centre of Finland (VTT); 2001 p.IST-2001-34372

APPENDIX A: EXPERIMENTALLY OBTAINED HUMAN RUNNING DATA

The names of the test subjects are Onur Ferhanoglu, Fatih Senbabaoglu and Gokhan Hatipoglu. At each presented data below, the subjects names are wirtten above each data. By this way, a comparision may be possible. The accelerometer is placed on the subject's hip area. The walking and running speeds are 3 km/h, 9 km/h, 15 km/h and 20 km/h. The x axis is time in "seconds" and the y axis is hip acceleration in "g".

I. Walking speed: 3 km/h

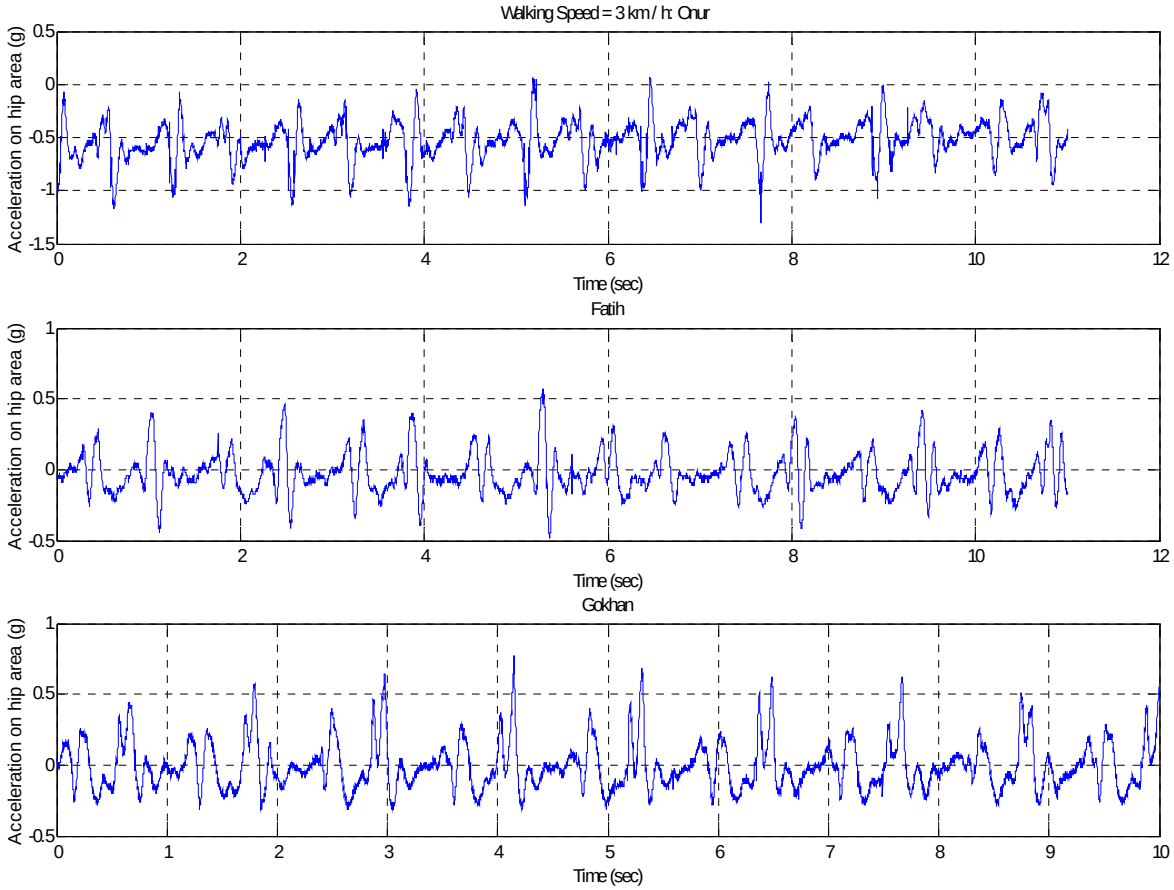

Figure A-1 Human hip acceleration for 3 km /h walking speed.

II. Jogging speed: 9 km/h

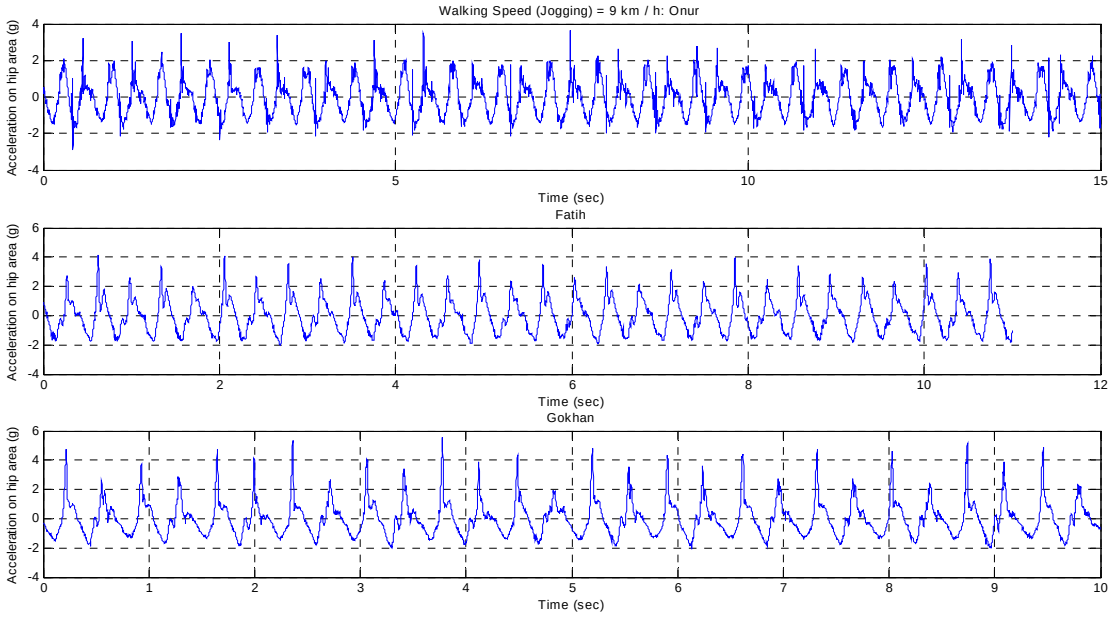

Figure A-2 Human hip acceleration for 9 km /h jogging speed.

III. Running speed: 15 km/h

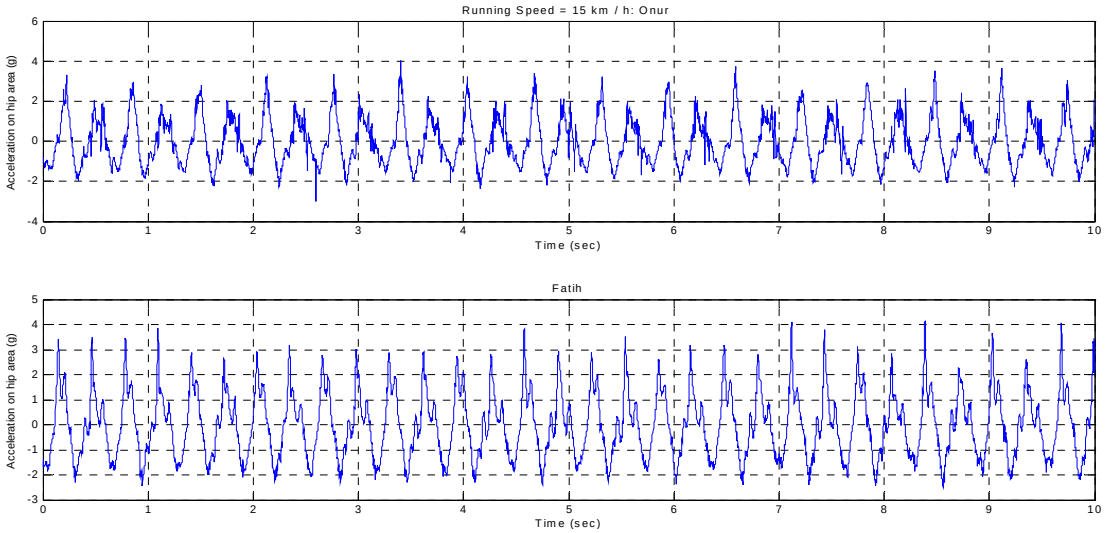

Figure A-3 Human hip acceleration for 15 km /h fast running speed.

IV. Outrun speed: 20 km/h

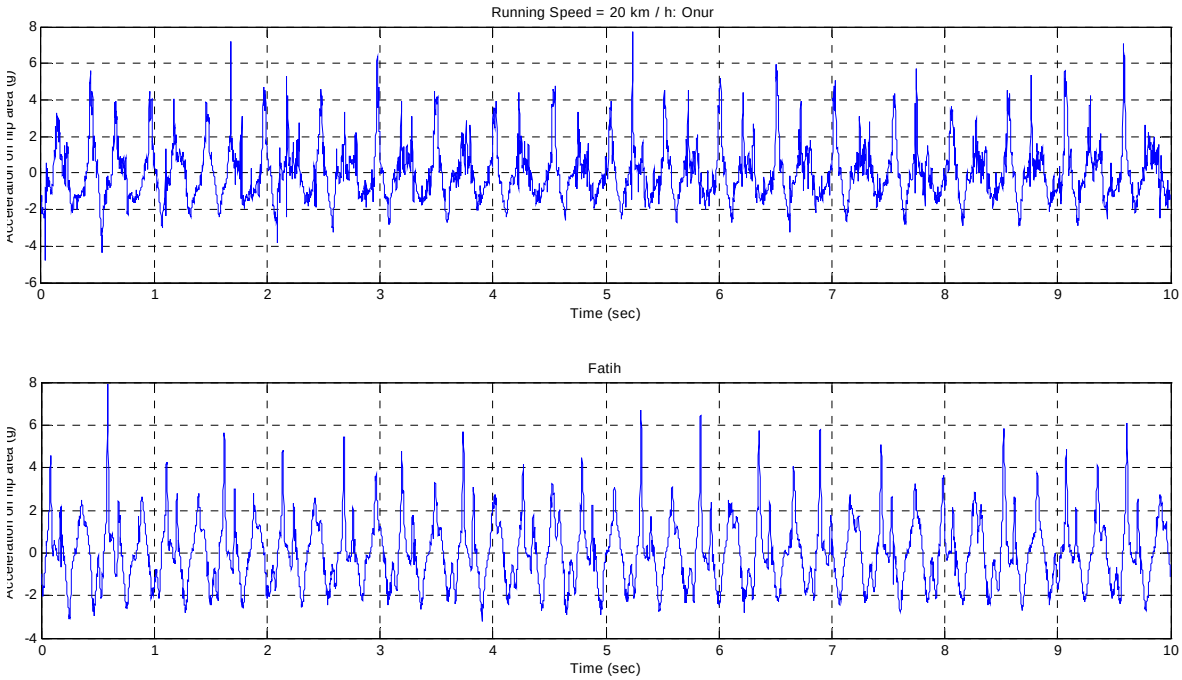

Figure A-4 Human hip acceleration for 20 km /h outrun speed.

VITA

Gokhan Hatipoglu was born in Istanbul, Turkey in 1984. He received his BSc. in Mechanical Engineering from Koc University in 2007. In order to pursue Msc. in Mechanical Engineering, he joined to Optical MEMS Laboratory (OML) of Koc University. He has received TUBITAK doctoral scholarship in order to pursue his PhD. degree in Electrical Engineering department of Pennsylvania State University, USA.

Gokhan Hatipoglu is a member of IEEE.